JOURNAL OF PETROLOGY | VOLUME 47 | NUMBER 2 | PAGES 355–383 | 2006 | doi:10.1093/petrology/egi078

Roles of Melting and Metasomatism in the Formation of the Lithospheric Mantle beneath the Leizhou Peninsula, South China

JIN-HAI YU[1,2]*, SUZANNE Y. O'REILLY[2], MING ZHANG[2], W. L. GRIFFIN[2,3] AND XISHENG XU[1,2]

[1]STATE KEY LABORATORY FOR MINERAL DEPOSITS RESEARCH, DEPARTMENT OF EARTH SCIENCES, NANJING UNIVERSITY, NANJING 210093, P.R. CHINA

[2]GEMOC ARC NATIONAL KEY CENTRE, DEPARTMENT OF EARTH AND PLANETARY SCIENCES, MACQUARIE UNIVERSITY, SYDNEY, N.S.W. 2109, AUSTRALIA

[3]CSIRO EXPLORATION AND MINING, NORTH RYDE, N.S.W. 2113, AUSTRALIA

RECEIVED JUNE 16, 2004; ACCEPTED SEPTEMBER 20, 2005
ADVANCE ACCESS PUBLICATION OCTOBER 20, 2005

This study characterizes the nature of fluid interaction and melting processes in the lithospheric mantle beneath the Yingfengling and Tianyang volcanoes, Leizhou Peninsula, South China, using in situ *trace-element analyses of clinopyroxene, amphibole and garnet from a suite of mantle-derived xenoliths. Clinopyroxenes from discrete spinel lherzolites exhibit large compositional variations ranging from extremely light rare earth element (LREE)-depleted to LREE-enriched. Trace-element modelling for depleted samples indicates that the Leizhou lherzolites are the residues of a mantle peridotite source after extraction of ~1–11% melt generated by incremental melting in the spinel lherzolite field with the degree of melting increasing upwards from about 60 km to 30 km. This process is consistent with gradational melting at different depths in an upwelling asthenospheric column that subsequently cooled to form the current lithospheric mantle in this region. The calculated melt production rate of this column could generate mafic crust 5–6 km thick, which would account for most of the present-day lower crust. The formation of the lithospheric column is inferred to be related to Mesozoic lithosphere thinning. Al-augite pyroxenites occur in composite xenoliths; these are geochemically similar to HIMU-type ocean island basalt. These pyroxenites postdate the lithospheric column formation and belong to two episodes of magmatism. Early magmatism (forming metapyroxenites) is inferred to have occurred during the opening of the South China Sea Basin (32–15 Ma), whereas the most recent magmatic episode (producing pyroxenites with igneous microstructures) occurred shortly before the eruption of the host magmas (6–0·3 Ma). Trace-element traverses from the contacts of the Al-augite pyroxenite with the spinel peridotite wall-rock in composite xenoliths record gradients in the strength and nature of metasomatic effects away from the contact, showing that equilibrium was not attained. Significant enrichment in highly incompatible elements close to the contacts, with only slight enrichment in Sr, LREE and Nb away from the contact, is inferred to reflect the different diffusion rates of specific trace elements. The observed geochemical gradients in metasomatic zones show that Sr, La, Ce and Nb have the highest diffusion rates, other REE are intermediate, and Zr, Hf and Ti have the lowest diffusion rates. Lower diffusion rates observed for Nb, Zr, Hf and Ti compared with REE may cause high field strength element (HFSE) negative anomalies in metasomatized peridotites. Therefore, metasomatized lherzolites with HFSE negative anomalies do not necessarily require a carbonatitic metasomatizing agent.*

KEY WORDS: *China; lithosphere; mantle xenoliths; clinopyroxene trace elements; mantle partial melting; mantle metasomatism; trace-element diffusion rates*

INTRODUCTION

The lithospheric mantle commonly experiences a long and complex geological history and exhibits extensive horizontal and vertical heterogeneities. Mantle peridotite

*Corresponding author. Fax: + 86 25 8368 6016. E-mail: jhyu@nju.edu.cn

and pyroxenite xenoliths provide the best window to understand the nature of the mantle and its depletion and fluid movement processes. It has been documented that melt extraction and metasomatism are two of the most important processes influencing the composition of lithospheric mantle (e.g. Zangana *et al.*, 1999; Xu *et al.*, 2000; Fodor *et al.*, 2002). Using the trace-element composition of depleted peridotites, the partial melting style and degree of melting occurring in mantle peridotites have been modelled (e.g. Johnson *et al.*, 1990; Niu, 1997; Norman, 1998; Xu *et al.*, 2000). The composition of metasomatized peridotites has been used to reveal the nature of enrichment processes and the geochemical signature of metasomatic agents (Menzies *et al.*, 1987; O'Reilly & Griffin, 1988; Rudnick *et al.*, 1993; Baker *et al.*, 1998; Gorring & Kay, 2000; Wang & Gasparik, 2001). In fact, many lithospheric mantle regions record several episodes of both partial melting and metasomatic overprints (Zangana *et al.*, 1999; Xu *et al.*, 2000). In addition, highly depleted peridotites record generally stronger metasomatism in their clinopyroxene (e.g. Frey & Green, 1974; O'Reilly & Griffin, 1988; Grégoire *et al.*, 2000). Metasomatism can change, to varying degrees, the trace-element composition of peridotites even for the weakly incompatible elements or compatible elements, such as Sc, Y and Yb (Norman, 1998; Grégoire *et al.*, 2000). In such cases, modelling partial melting processes using these elements without consideration of metasomatic effects may lead to false conclusions.

In recent studies of mantle metasomatism, the most common approach to defining the nature of metasomatic agents has been to use the partition coefficient between minerals and melt and mineral compositions. However, trace elements may have different diffusion properties depending on specific physico-chemical conditions (Zanetti *et al.*, 1996). In weak metasomatism some elements with low diffusivity may not achieve equilibrium between the peridotite wall-rocks and metasomatic agents. On the other hand, the difference in partition coefficients for mineral/basaltic melt ($D_{min/bas}$) and mineral/carbonatite melt ($D_{min/carb}$) is relevant only for high field strength elements (HFSE) (Hart & Dunn, 1993; Klemme *et al.*, 1995; Vannucci *et al.*, 1998). Therefore, it is very important to seek other evidence to characterize the metasomatic agent.

The suite of xenoliths in this study comprises discrete lherzolites and composite xenoliths (lherzolite with pyroxenite) from the Yingfengling and Tianyang volcanoes of the Leizhou Peninsula, South China, and includes enriched as well as depleted peridotites, and particularly important composite xenoliths. This suite of xenoliths provides an excellent natural compositional range of Cr-diopside mantle wall-rocks that come from a large depth range and show many contact relationships with inferred mantle melt veins (Al-augite rock types), thus allowing detailed exploration of metasomatic processes.

In a previous paper (Yu *et al.*, 2003*a*), we classified this suite of xenoliths and other discrete metapyroxenites and megacrystic aggregates according to their petrographic and mineral chemical features, calculated their equilibrium temperature and/or pressure conditions, constructed the paleogeotherm based on data from the garnet websterites, demonstrated a high heat flow (from both the geotherm and geophysical data), and confirmed the lithospheric rock-type section for the Leizhou region and the thickness of crust (30 km) and lithosphere (100 km) by integration of the xenolith information with seismic data. In this study, detailed trace-element data for clinopyroxenes, amphiboles and garnets from the range of xenolith types have been obtained by *in situ* laser-ablation inductively coupled plasma mass spectrometry (LA-ICPMS). These clinopyroxene compositions are then used to discuss partial melting processes recorded in the depleted lherzolites, to characterize the nature of the metasomatic processes, and especially to evaluate the diffusion rate of different trace elements and the resultant effect on the geochemical signatures and patterns of metasomatized lherzolites. In addition, we provide a geodynamic framework for the evolution of the lithospheric mantle in this region.

GEOLOGICAL BACKGROUND

The Leizhou Peninsula and the nearby Hainan Island are located at the southernmost margin of South China continent and the northern edge of the South China Sea Basin (SCSB) (Fig. 1). There are extensive Cenozoic basalt eruptions spreading over this area and surrounding regions, such as in Vietnam and Thailand. These intracontinental volcanic rocks surrounding the SCSB, and those from seamounts within the SCSB, are commonly younger than the SCSB sea-floor extension, i.e. they are post-spreading volcanic rocks, and consist mainly of quartz tholeiite and olivine tholeiite (dominant in early eruptive series), with minor alkali basalts (increasing in later eruptive series: Flower *et al.*, 1992; Hoang & Flower, 1998). These latter basalts are characterized by depleted Sr–Nd isotopic, Dupal-like Pb isotopic compositions and enriched ocean island basalt (OIB)-type incompatible-element distributions, suggesting the interaction of asthenosphere with subcontinental lithosphere (Zhu & Wang, 1989; Flower *et al.*, 1992; Tu *et al.*, 1992). Isotopic data for these post-spreading basalts indicate the mantle source heterogeneity, reflecting mixing of EM2 and normal mid-ocean ridge basalt (N-MORB) mantle reservoirs. However, enriched trace-element composition and depleted Sr–Nd isotopic compositions suggest that partial melting of this mantle has probably taken place shortly after mantle metasomatism.

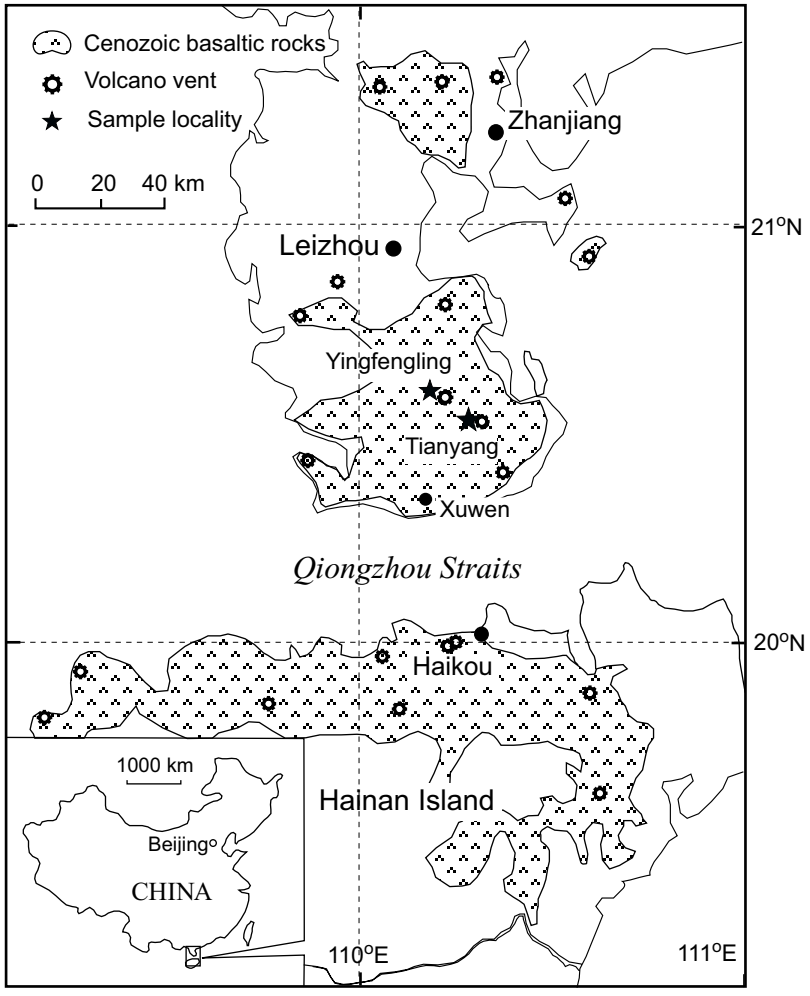

Fig. 1. Sample locations and distribution of Cenozoic basaltic volcanoes in the Leizhou–Hainan area, South China.

The SCSB was opened from late Oligocene to middle Miocene (32 to 15·5 Ma, Taylor & Hayes, 1983; Briais *et al.*, 1993), almost simultaneously with the tectonic extrusion of Indochina along the Red River fault as a result of the northward collision of India with Eurasia (Harrison *et al.*, 1996; Wang *et al.*, 1998). Therefore, some workers interpret the SCSB opening as the result of the southeastward extrusion of Indochina (Tapponnier *et al.*, 1986; Briais *et al.*, 1993), although others believe that the SCSB opening was simply initiated by the extension independent of the tectonic extrusion (Chung *et al.*, 1997; Wang *et al.*, 1998).

Seismic data for South China and the SCSB exhibit significant lithospheric structural changes and obvious thinning of crustal thickness from the northern continental margin to the centre of the SCSB (from 28 km to 8 km; Lin *et al.*, 1988; Yao *et al.*, 1994; Yan *et al.*, 2001). The lower-crust thickness also decreases from the northern margin to the basin centre (Yan *et al.*, 2001), suggesting that the lower crust formed prior to the basin pull-apart. The lithosphere of South China is thin; the old lithosphere appears to have been removed and replaced by new upwelling mantle, which took probably place during the Mesozoic (Xu *et al.*, 2000). Studies on the granulite xenoliths from South China indicate that lower crustal mafic granulites were dominantly formed by Mesozoic basalt underplating (e.g. Yu *et al.*, 2003*c*). Geological and geophysical data show only a small amount of magma intruded or erupted during the South China Sea opening (Yan *et al.*, 2001), whereas extensive volcanism took place after the cessation of the SCSB floor spreading.

XENOLITH PETROGRAPHY

The studied xenolith samples were collected from Yingfengling and Tianyang basaltic volcanoes, 15 km apart, in the centre of the Leizhou Peninsula (Fig. 1). These two post-spreading Cenozoic volcanic vents are composed of several layers of lava and breccia, and interlayered

sediments. The lavas are dated from 6·1 Ma to 0·3 Ma (from base to top: Zhu & Wang, 1989; Xu *et al.*, 1999). The xenoliths from the Yingfengling volcano represent a wide range of rock types, 2–10 cm across, and angular or subangular in shape, whereas those from the Tianyang volcano are peridotites generally 20 cm across with rounded shapes. The xenolith suite includes anhydrous Cr-diopside spinel lherzolites, spinel websterites, layered Cr-diopside xenoliths, and composite Al-augite–Cr-diopside spinel xenoliths (Table 1). Discrete Cr-diopside sp-lherzolites have large modal variations with 44·2–70·8% olivine, 15·1–37·2% orthopyroxene, 6·2–28·7% Cr-diopside and 0·7–3·6% spinel. Sp-websterites contain mainly orthopyroxene (38·5–50·5%) and Cr-diopside (45·0–57·8%). Layered Cr-diopside xenoliths consist of sp-lherzolite and sp-websterite. Al-augite composite xenoliths comprise sp-lherzolite domains in contact with Al-augite pyroxenite or very coarse-grained mafic assemblages referred to here as megacrystic aggregates that have been described in detail by Yu & O'Reilly (2001) and Yu *et al.* (2003*a*, 2003*b*) and listed in Table 1. The megacrystic aggregate in composite xenolith Lz-17 consists of Al-augite, Mg-, Ca-rich almandine, oligoclase and ilmenite, with rare small grains of biotite (~0·04 mm long) occurring as inclusions in ilmenite. The megacrystic aggregate in sample Lz-29 consists of medium-grained Al-augite, Mg-, Ca-rich almandine, ilmenite and apatite (Yu & O'Reilly, 2001; Yu *et al.*, 2003*b*).

Amphibole occurs as interstitial grains or as rims on spinel in lherzolite and is mainly confined to the composite xenoliths indicating a metasomatic origin. Discrete sp-lherzolite Lz-21 also contains amphibole (0·4%) and its low Mg-number indicates modal metasomatism.

Detailed major-element compositions of minerals from these xenoliths have been reported by Yu *et al.* (2003*a*). Most discrete lherzolites have similar major element compositions with high Mg-number of olivine (89·5–90·4), orthopyroxene (90·0–90·8), and clinopyroxene (89·7–91·9) (Table 1). Samples Lz-7 and Lz-21 have lower Mg-number, and Lz-7 shows large compositional variation on a centimeter scale with, for example, Mg-number in clinopyroxene ranging from 84·7 to 89·8. Sp-websterites exhibit similar mineral compositions to Cr-diopside sp-lherzolite, except for lower Cr-number of spinel. The minerals in the layered sp-lherzolite and sp-websterite domains of Cr-diopside composite xenoliths have identical mineral compositions indistinguishable from those of the discrete lherzolites and websterites. Minerals from Al-augite composite xenoliths have very low Mg-number and marked compositional variations, especially in lherzolite–megacryst aggregate composites (Table 1).

Temperatures of these xenoliths calculated by the Brey & Köhler (1990) two-pyroxene thermometer range from 870°C to 1130°C, spanning a depth range from 63 to 30 km when applied to the xenolith-derived geotherm for this region (Yu *et al.*, 2003*a*). Sp-websterites, layered Cr-diopside xenoliths and spinel lherzolites with high-Mg clinopyroxene (Table 1) have the lowest temperatures (870–950°C) and are inferred to come from shallower levels (28–37 km). Al-augite composites generally have higher temperatures and thus occur deeper in the section. Identical calculated temperatures for metapyroxenite and lherzolite rock types in some composite xenoliths indicate thermal equilibrium (Table 1).

ANALYTICAL TECHNIQUES

Olivine, orthopyroxene, diopside and spinel separates were hand-picked from coarsely crushed Cr-diopside sp-lherzolite xenoliths. These grains were mounted and polished for analysis by electron microprobe and LA-ICPMS. Polished sections 100 μm thick were also made for layered and composite xenoliths. Concentrations of 31 trace elements (Sc, Ti, V, Co, Ni, Zn, Ga, Rb, Sr, Y, Zr, Nb, Ba, REE, Hf, Pb, Th and U) for clinopyroxene, amphibole and garnet (Tables 2 and 3) were determined *in situ* by LA-ICPMS with a Perkin Elmer Elan 6000 instrument in the GEMOC National Key Centre laboratories at Macquarie University, Australia. Analytical procedure and precision are the same as those described in detail by Grégoire *et al.* (2000) and Xu *et al.* (2000). Almost all clinopyroxenes have Rb abundances below the detection limit (0·1 ppm), so are not listed in Table 2.

At least five points were analysed for clinopyroxene grains in each discrete Cr-diopside sp-lherzolite and sp-websterite sample, and more than 13 points for grains in composite xenoliths (up to 41 points for Lz-10) to cover grains across the whole section or for a coverage of 5–7 cm^2 for mounted grains in order to assess homogeneity. Analyses show that clinopyroxene compositions in most discrete Cr-diopside lherzolites, sp-websterites and layered Cr-diopside xenoliths are homogeneous, except for those from Cr-diopside lherzolites Lz-7 and Lz-21. Clinopyroxenes from these two lherzolites have large trace-element abundance variations, with Mg-number varying on a centimeter scale, similar to the clinopyroxene Mg-number variation for composite xenoliths. This indicates that these samples were close to pyroxenite veins and accordingly metasomatized, and thus they are described together with the composite xenoliths below.

TRACE-ELEMENT COMPOSITIONS OF CLINOPYROXENES

Transition metals

Clinopyroxenes from discrete Leizhou Cr-diopside lherzolites have relatively uniform Sc (55·2–69·2 ppm),

Table 1: Mineral Mg-number and Cr-number (for spinel only) and calculated temperatures of Leizhou xenoliths

		ol	opx	cpx	sp Mg-no.	sp Cr-no.	amp	grt	others	*T* (°C)	EOM
Discrete Cr-diopside spinel lherzolites											
xw97-1		90·4	90·8	90·8	77·9	13·8				1073	W
xw97-2		89·5	90·0	90·5	77·7	8·4				910	
xw97-3		89·7	90·3	91·1	78·3	9·6				1018	W
xw97-4		89·8	90·2	89·9	77·1	10·8				1088	
xw97-5		89·9	90·4	90·3	77·9	11·2				1074	
xw97-8		90·1	90·6	90·7	78·5	11·1				1063	
Lz-2		90·2	90·6	90·2	77·8	12·5				1105	S
Lz-3		89·7	90·3	90·9	78·3	10·4				959	
Lz-5		89·8	90·1	91·7	74·3	13·9				871	
Lz-6		89·7	90·2	91·2	78·2	9·6				955	
Lz-8		90·2	90·6	90·0	77·9	11·4				1113	M
Lz-9		90·3	90·7	90·2	77·9	12·4				1129	S
Lz-11		90·3	90·8	91·9	77·7	13·9				990	W
Lz-12		90·0	90·3	89·7	75·9	15·0				1137	M
Lz-7	Mg-rich zone	88·4	89·0	89·0	73·5	13·1				1069	W
Lz-7	Fe-rich zone	85·4	85·3	86·1	66·6	14·0				1056	S
Lz-21	Mg-rich zone	86·9	87·5	87·0	70·5	10·2	83·3			1079	M
Lz-21	Fe-rich zone	86·3	87·3	86·6	69·3	10·4	82·4			1079	M
Discrete spinel websterites											
Lz-32			89·1	90·6	79·1	3·5				901	
Lz-35			89·9	91·1	77·2	8·9				915	
Lz-40			89·5	90·9	77·6	8·6				922	
Lz-41			89·6	91·1	78·1	7·6				918	
Layered Cr-diopside xenoliths											
Lz-18	sp-lherzolite	89·6	90·2	91·3	77·7	8·6				930	
	sp-websterite		90·1	91·1	77·4	8·8				916	
Lz-19	sp-lherzolite	89·8	90·4	91·2	78·7	8·2				952	
	sp-websterite		90·2	91·1	78·1	7·6	89·0			946	
Al-augite composite xenoliths											
Cr-diopside lherzolite and metapyroxenite components of composite xenoliths											
Lz-1	sp-lherzolite	89·6	90·0	89·5	73·4	17·0				1130	S
	transition zone		90·0	88·7	75·0	13·0				1122	
	metapyroxenite		89·9	88·6						1111	
Lz-10	sp-lherzolite	86·4	87·1	85·5	70·6	9·2				1131	S
	metapyroxenite			83·4			81·3	78·1	ilm		
Lz-20	sp-lherzolite	84·0	84·9	83·9	65·3	8·5				1105	M
	metapyroxenite			83·5			80·9		ilm		
Lz-37	sp-lherzolite	84·2	85·4	85·0	63·2	11·8	82·2			1038	S
	amp-websterite		83·6	77·8			76·7		ilm	1063	
	gt-websterite		80·4	79·7				66·9	ilm	1026	
Spinel lherzolite and megacryst components of composite xenoliths											
Lz-17	sp-lherzolite	80·7	82·6	82·6					sp	1083	M
		75·2	78·7	73·9					sp		S
	reaction zone		74·4	72·1					ilm	1097	
	megacryst aggregate			56·8				40·1	pl, ilm, bt		
Lz-29	sp-lherzolite	80·2	79·9	79·4	51·5	11·8	76·1			1067	S
	transition zone	77·7	77·2				71·1		ilm		S
	transition zone		75·7	73·7				63·0	ilm	1074	
	megacryst aggregate			68·8				56·4	ap, ilm		
				65·7					ap, ilm		
				61·8					ap, ilm		

Mg-number = 100 × Mg/(Mg + Fe); Cr-number = 100 × Cr/(Cr + Al); *T* (°C), Brey & Köhler (1990) two-pyroxene thermometer (Yu *et al.*, 2003*a*); samples with prefix 'xw-' are from Tianyang, those with prefix 'Lz-' are from Yingfengling. EOM, extent of metasomatism of Cr-diopside lherzolites based on the trace-element characteristics of clinopyroxenes (S, strong; M, moderate; W, weak).

Table 2: Average trace-element concentrations of clinopyroxenes from Leizhou xenoliths (ppm)

	discrete spinel lherzolite												
	xw97-1	xw97-2	xw97-3	xw97-4	xw97-5	xw97-8	Lz-2	Lz-3	Lz-5	Lz-6	Lz-8	Lz-9	Lz-11
av.-no.	8	7	9	8	9	9	6	6	7	5	6	5	5
Mg-no.	90·8	90·5	91·1	89·9	90·3	90·7	90·2	90·9	91·7	91·2	90·0	90·2	91·9
Sc	60·6	60·2	61·1	59·0	58·8	60·0	56·4	64·1	69·2	60·6	57·8	53·7	66·8
Ti	1725	3345	1802	3157	3292	3094	2550	3201	1871	1850	2806	2566	1216
V	237	257	241	242	265	254	235	264	249	252	245	241	250
Co	22·6	18·2	22·6	21·1	21·6	21·6	23·5	18·8	18·3	18·6	23·5	23·6	20·2
Ni	369	289	371	325	338	341	371	308	282	302	374	383	331
Zn	10·1	4·80	9·27	8·16	9·52	10·4	9·20	6·08	5·21	7·14	9·70	10·5	7·48
Ga	3·32	4·43	3·39	4·21	4·22	4·30	4·17	3·95	3·56	3·82	4·15	4·36	2·86
Sr	24·7	67·0	24·9	86·6	85·5	74·4	143	66·4	40·4	11·8	101	138	10·4
Y	14·9	20·4	15·7	17·8	16·7	17·8	15·0	19·8	16·0	17·0	18·4	14·5	13·0
Zr	10·7	33·8	11·8	33·3	32·1	32·9	27·2	33·1	16·7	5·98	35·2	26·0	2·64
Nb	0·41	0·047	0·38	0·28	0·28	0·15	1·12	0·16	0·17	0·15	0·70	1·03	0·45
Ba	0·30	0·40	b.d.	0·28	b.d.	b.d.	b.d.	b.d.	b.d.	b.d.	0·37	0·80	b.d.
La	0·82	0·67	0·84	1·60	1·47	1·05	4·25	1·30	0·60	0·14	2·72	4·02	0·47
Ce	1·63	2·80	1·70	4·14	4·27	3·57	13·1	3·82	1·84	0·53	5·72	13·1	0·69
Pr	0·23	0·59	0·25	0·66	0·72	0·63	2·15	0·68	0·33	0·14	0·83	2·12	0·09
Nd	1·42	3·97	1·63	3·84	4·19	3·89	11·2	4·22	2·31	1·30	4·53	11·1	0·70
Sm	0·91	1·73	0·97	1·60	1·64	1·68	3·33	1·67	1·11	0·92	1·83	2·98	0·54
Eu	0·42	0·77	0·45	0·72	0·68	0·69	1·32	0·75	0·52	0·45	0·81	1·10	0·27
Gd	1·58	2·66	1·83	2·37	2·36	2·23	3·37	2·62	1·91	1·72	2·60	2·94	1·18
Tb	0·32	0·51	0·37	0·45	0·45	0·46	0·50	0·51	0·41	0·40	0·51	0·48	0·29
Dy	2·40	3·51	2·69	3·30	3·07	3·14	3·18	3·58	2·80	2·82	3·28	2·84	1·83
Ho	0·58	0·79	0·64	0·73	0·68	0·68	0·59	0·80	0·67	0·67	0·74	0·58	0·50
Er	1·60	2·31	1·78	1·99	1·82	1·88	1·70	2·15	1·90	1·98	1·97	1·50	1·52
Tm	0·25	0·33	0·27	0·28	0·25	0·28	0·24	0·33	0·27	0·28	0·29	0·20	0·20
Yb	1·63	2·23	1·82	2·01	1·78	1·89	1·48	2·20	1·83	1·96	1·88	1·44	1·54
Lu	0·23	0·31	0·24	0·25	0·24	0·27	0·19	0·31	0·25	0·30	0·25	0·20	0·22
Hf	0·50	1·04	0·52	1·14	1·04	0·96	0·90	1·12	0·64	0·38	1·08	0·84	0·18
Pb	b.d.	0·30	0·12	b.d.	b.d.	0·22	0·23	0·28	0·22	b.d.	0·20	b.d.	0·23
Th	0·17	b.d.	0·19	0·081	0·090	0·028	0·070	0·34	b.d.	0·030	0·22	0·064	0·048
U	0·033	b.d.	0·039	0·030	0·030	0·019	0·035	0·122	0·024	b.d.	0·068	0·030	b.d.
$(La/Pr)_n$	1·37	0·43	1·30	0·92	0·77	0·63	0·75	0·72	0·68	0·38	1·24	0·72	1·90
$(La/Yb)_n$	0·35	0·21	0·32	0·55	0·57	0·38	1·98	0·41	0·23	0·05	1·00	1·93	0·21
Sr/Sr*	1·11	1·31	1·02	1·48	1·37	1·35	0·81	1·11	1·30	0·82	1·37	0·78	1·02
Ti/Ti*	0·51	0·56	0·48	0·58	0·62	0·60	0·29	0·55	0·45	0·50	0·46	0·34	0·51
Zr/Zr*	0·61	0·87	0·61	0·90	0·83	0·86	0·30	0·84	0·69	0·34	0·82	0·30	0·27
Nb/Nb*	0·44	0·13	0·37	0·22	0·23	0·18	0·41	0·06	0·25		0·28	0·40	

V (237–265 ppm), Co (18·3–23·5 ppm) and Ni contents (282–373 ppm) (Table 2). Because of their similarity in these and other trace elements (see below), discrete Cr-diopside lherzolites, Cr-diopside sp-websterites and layered Cr-diopside xenoliths are considered together (Fig. 2).

Sc contents of clinopyroxenes from Al-augite composite xenoliths are significantly lower than those from Cr-diopside suite xenoliths, and decrease from lherzolite to pyroxenite domains with decreasing Mg-number (Table 2, Fig. 2a). V abundances are similar to those of the Cr-diopside suite xenoliths (Fig. 2b). Clinopyroxenes

Table 2: continued

	discrete sp lherz.	layered xenolith		spinel websterite				spinel lherzolite				
	Lz-12	Lz-18	Lz-19	Lz-32	Lz-35	Lz-40	Lz-41	Lz-7				
av.-no.	9	10	6	6	7	11	11	1	2	9	1	2
Mg-no.	89·7	91·3	91·2	90·6	91·1	90·9	91·1	89·2	88·6	86·8	85·6	84·7
Sc	55·2	61·0	60·0	62·4	53·4	51·5	54·5	59·2	58·3	60·8	58·6	49·1
Ti	2187	2759	3075	3583	2992	2965	2973	2283	2327	2383	2366	4243
V	243	252	253	339	239	240	242	231	236	241	234	213
Co	23·3	17·1	18·3	17·7	17·8	18·8	18·6	20·6	20·2	21·8	23·6	24·3
Ni	371	275	293	325	329	358	356	318	311	326	323	300
Zn	11·0	4·88	5·08	4·87	3·70	4·08	3·69	16·0	17·4	17·5	20·8	22·5
Ga	4·12	4·11	4·18	4·42	4·40	4·83	4·70	4·10	3·65	3·77	4·70	9·40
Sr	107	61·1	59·1	48·3	60·8	61·6	60·3	69·8	105	120	116	108
Y	14·6	19·4	19·8	20·9	18·8	18·6	18·3	17·3	16·3	16·4	16·2	12·4
Zr	24·1	26·7	28·1	28·3	27·9	27·4	26·8	26·5	26·8	29·2	32·8	58·7
Nb	1·37	0·10	0·12	0·11	0·14	0·13	0·15	0·69	0·73	0·71	0·71	0·64
Ba	0·23	b.d.	b.d.	b.d.	9·35	b.d.	0·15	b.d.	0·20	0·27	b.d.	0·40
La	3·37	0·64	0·92	1·02	0·95	0·90	0·90	1·80	3·30	3·86	4·30	4·50
Ce	6·66	2·56	3·63	3·77	3·79	3·73	3·69	3·60	6·25	7·92	9·50	13·10
Pr	0·83	0·51	0·71	0·67	0·71	0·73	0·71	0·57	0·70	0·96	1·30	2·40
Nd	4·40	3·40	4·45	4·05	4·34	4·39	4·46	3·40	3·95	4·87	5·70	12·15
Sm	1·48	1·52	1·80	1·80	1·82	1·75	1·73	1·40	1·40	1·62	1·90	4·05
Eu	0·61	0·68	0·80	0·73	0·73	0·78	0·75	0·73	0·63	0·73	0·82	1·60
Gd	2·02	2·44	2·63	2·58	2·55	2·59	2·54	2·20	2·10	2·29	2·50	4·60
Tb	0·40	0·47	0·51	0·52	0·47	0·47	0·48	0·42	0·43	0·43	0·35	0·55
Dy	2·63	3·48	3·50	3·58	3·37	3·32	3·22	3·20	2·95	2·89	2·90	3·55
Ho	0·57	0·74	0·78	0·83	0·76	0·74	0·73	0·69	0·69	0·67	0·72	0·60
Er	1·62	2·17	2·18	2·37	2·00	2·04	2·05	1·90	1·85	1·76	1·80	1·40
Tm	0·23	0·32	0·32	0·36	0·30	0·28	0·28	0·26	0·25	0·27	0·22	0·15
Yb	1·50	2·10	2·03	2·38	1·96	1·97	1·95	2·00	1·75	1·79	1·80	1·10
Lu	0·21	0·30	0·29	0·33	0·25	0·26	0·27	0·30	0·22	0·24	0·22	0·14
Hf	0·74	0·81	0·94	0·93	0·91	0·94	0·83	0·60	0·70	0·91	0·80	1·40
Pb	0·00	0·19	0·11	0·11	0·55	0·16	0·15	b.d.	0·20	0·25	0·26	0·18
Th	0·098	0·019	0·020	0·015	0·070	0·024	0·030	0·27	0·30	0·34	0·27	0·22
U	0·038	0·014	b.d.	0·017	0·030	0·011	0·013	0·080	0·060	0·068	0·060	0·050
$(La/Pr)_n$	1·53	0·47	0·49	0·58	0·50	0·47	0·48	1·20	1·79	1·52	1·25	0·71
$(La/Yb)_n$	1·55	0·21	0·31	0·30	0·33	0·32	0·32	0·62	1·30	1·49	1·65	2·83
Sr/Sr*	1·35	1·36	0·98	0·83	1·01	1·02	0·99	1·36	1·45	1·32	1·08	0·58
Ti/Ti*	0·47	0·51	0·51	0·62	0·52	0·50	0·52	0·43	0·49	0·44	0·39	0·37
Zr/Zr*	0·64	0·78	0·67	0·70	0·67	0·66	0·65	0·82	0·77	0·70	0·68	0·57
Nb/Nb*	0·59	0·18		0·14	0·15	0·21	0·22	0·32	0·28	0·23	0·23	0·20

in Al-augite composite lherzolites have higher Co contents than those in Cr-diopside suite xenoliths; pyroxenite domains have the highest Co values, especially in megacrystic aggregate–lherzolite composites (Lz-17 and Lz-29; Fig. 2c). Clinopyroxenes of most Al-augite composites display similar Ni contents to those from Cr-diopside suite xenoliths, with a slight decrease in Ni from lherzolite to pyroxenite. In megacrystic rock types Lz-17 and Lz-29, the Ni content of clinopyroxene is very low (Fig. 2d).

In the plots of Mg-number vs transition metals, Sc and Mg-number correlate positively, and Ni and Mg-number negatively in the Cr-diopside suite xenoliths (Fig. 2).

Table 2: continued

	spinel lherzolite				lherzolite		pyroxenite	spinel lherzolite			pyroxenite	
	Lz-21				Lz-1		Lz-1	Lz-20			Lz-20	
av.-no.	1	3	4	5	3	1	3	1	3	3	3	4
Mg-no.	87·1	86·8	86·7	86·6	89·5	88·7	88·6	84·2	84·0	84·0	83·6	83·4
Sc	56·7	57·6	50·2	47·5	43·8	40·7	40·3	55·3	47·3	42·2	34·5	18·8
Ti	2832	3295	4511	5656	8661	10136	11170	3444	4760	5722	8430	12308
V	237	242	241	247	220	212	224	255	237	240	250	281
Co	23·5	24·5	25·2	24·9	25·5	23·8	25·6	26·6	27·9	28·7	27·6	27·5
Ni	324	321	318	312	412	392	414	347	352	351	330	289
Zn	14·0	13·9	13·6	14·0	13·7	14·1	13·1	21·4	25·7	25·9	25·0	22·7
Ga	4·30	5·77	7·16	7·63	6·93	7·30	8·50	4·90	6·55	7·77	10·3	15·4
Sr	147	171	177	188	138	149	148	124	138	132	123	123
Y	17·0	16·0	14·3	12·8	16·4	17·1	18·9	16·6	14·5	13·4	11·3	11·1
Zr	33·9	42·1	55·3	68·5	46·5	58·3	65·6	37·1	56·3	59·8	68·8	87·2
Nb	0·74	0·58	0·53	0·55	1·37	1·80	2·13	0·76	0·80	0·86	0·91	1·31
Ba	b.d.	b.d.	0·19	0·26	b.d.	b.d.	0·26	0·19	0·25	b.d.	b.d.	b.d.
La	4·30	4·77	4·82	5·15	5·60	6·10	6·43	3·40	3·75	3·90	4·07	4·65
Ce	10·4	11·8	12·2	13·4	20·4	22·7	23·9	9·50	12·1	12·3	12·4	13·9
Pr	1·40	1·73	1·72	1·90	3·40	3·80	4·10	1·31	1·93	2·06	2·06	2·38
Nd	5·90	8·20	8·98	10·6	18·7	21·7	24·1	6·40	10·6	11·6	11·9	13·7
Sm	1·80	2·43	2·89	3·40	4·97	6·00	7·23	1·90	3·30	3·80	4·30	5·00
Eu	0·74	1·01	1·24	1·27	1·80	2·10	2·60	0·79	1·30	1·45	1·64	1·95
Gd	2·40	3·13	3·15	3·35	5·03	5·90	7·37	2·60	3·50	3·90	4·27	5·23
Tb	0·39	0·48	0·50	0·52	0·70	0·80	1·03	0·51	0·55	0·59	0·63	0·70
Dy	3·20	3·17	2·98	2·93	3·83	4·30	5·10	2·70	3·15	3·10	3·10	3·18
Ho	0·67	0·64	0·57	0·54	0·65	0·66	0·75	0·72	0·62	0·55	0·47	0·47
Er	1·90	1·70	1·47	1·38	1·53	1·40	1·57	1·90	1·54	1·38	0·97	0·91
Tm	0·28	0·24	0·19	0·18	0·20	0·22	0·20	0·25	0·19	0·16	0·12	0·10
Yb	1·90	1·63	1·34	1·10	1·33	1·30	1·23	1·80	1·36	1·12	0·80	0·70
Lu	0·31	0·26	0·17	0·15	0·19	0·19	0·16	0·25	0·20	0·15	0·12	0·095
Hf	1·00	1·07	1·30	1·73	1·77	2·10	2·33	1·03	1·29	1·60	1·97	3·28
Pb	b.d.	0·27	0·28	0·30	b.d.	b.d.	b.d.	0·16	b.d.	0·15	0·15	0·18
Th	0·41	0·39	0·42	0·41	0·060	0·080	0·077	0·14	0·16	0·16	0·16	0·22
U	0·130	0·110	0·096	0·095	0·040	b.d.	0·030	0·048	0·035	0·038	0·042	0·056
$(La/Pr)_n$	1·16	1·04	1·06	1·03	0·62	0·61	0·59	0·98	0·74	0·72	0·75	0·74
$(La/Yb)_n$	1·56	2·02	2·49	3·24	2·90	3·24	3·61	1·31	1·91	2·40	3·52	4·63
Sr/Sr*	1·27	1·19	1·16	1·08	0·48	0·46	0·42	1·09	0·84	0·75	0·69	0·61
Ti/Ti*	0·51	0·44	0·54	0·65	0·68	0·68	0·61	0·57	0·53	0·57	0·75	0·91
Zr/Zr*	0·70	0·64	0·74	0·77	0·33	0·35	0·34	0·72	0·65	0·61	0·65	0·71
Nb/Nb*	0·18	0·14	0·13	0·13	0·39	0·57	0·56	0·30	0·32	0·33	0·33	0·40

However, in each Al-augite composite xenolith, Mg-number in clinopyroxene correlates positively with both Sc and Ni, and negatively with Co (Fig. 2). It is worth noting that the Ni correlation in Cr-diopside suite xenoliths is opposite to that for Al-augite composite xenoliths (Fig. 2d). Ni in clinopyroxenes from Cr-diopside suite xenoliths is positively correlated with the temperature (Fig. 3a), which implies that Ni distribution in clinopyroxene of Cr-diopside suite xenoliths is probably controlled by temperature. Ni variation in Al-augite composite xenoliths is evidently the result of interaction of mafic melt and wall-rock Cr-diopside lherzolite.

Table 2: continued

	spinel lherzolite					garnet pyroxenite					spinel lherzolite	
	Lz-10					Lz-10					Lz-17	
av.-no.	3	8	2	4	7	7	2	3	2	3	4	5
Mg-no.	86·4	86·0	85·4	84·9	84·6	84·5	84·3	84·1	83·8	83·2	82·6	80·6
Sc	55·9	51·6	52·8	48·2	41·3	26·8	22·8	12·1	11·6	6·3	53·4	47·9
Ti	3280	4119	3734	4384	6763	11500	13158	13313	11370	12561	2113	2493
V	245	246	243	242	234	235	242	245	225	274	228	225
Co	24·4	26·2	26·0	26·2	25·7	24·8	27·2	23·2	28·8	30·9	29·9	36·3
Ni	331	335	354	351	317	281	279	238	259	244	312	270
Zn	16·7	17·7	15·7	19·1	16·5	14·5	19·8	11·2	22·0	21·7	36·3	57·4
Ga	5·07	6·58	5·98	6·87	8·56	12·1	14·7	14·6	21·0	26·5	4·72	5·92
Sr	98·9	103	104	105	103	107	112	109	116	126	104	106
Y	15·8	14·3	14·8	14·3	11·5	10·8	12·2	9·66	7·75	7·10	13·8	13·0
Zr	31·1	35·9	35·4	39·0	45·9	68·9	72·8	71·1	75·0	79·6	26·6	30·1
Nb	0·74	0·80	0·80	0·94	0·84	1·00	1·15	1·47	1·02	1·33	0·39	0·27
Ba	b.d.	b.d.	b.d.	0·12	b.d.	b.d.	b.d.	b.d.	b.d.	b.d.	0·50	0·63
La	2·77	3·16	3·16	3·27	3·17	3·63	3·80	3·80	3·55	3·90	2·85	2·80
Ce	7·50	8·66	8·69	9·09	9·19	10·5	10·7	11·8	11·3	12·3	6·63	7·84
Pr	1·03	1·33	1·36	1·47	1·53	1·75	1·75	1·94	2·00	2·23	0·86	1·21
Nd	5·67	7·31	7·48	8·26	8·70	10·7	10·8	11·2	12·7	14·0	4·18	6·10
Sm	1·90	2·45	2·56	2·85	3·13	3·89	4·20	4·47	4·75	5·20	1·59	2·06
Eu	0·80	0·99	1·00	1·15	1·21	1·54	1·60	1·70	1·85	1·93	0·67	0·87
Gd	2·47	2·84	2·71	3·05	3·27	4·16	4·40	4·63	4·80	4·97	1·88	2·37
Tb	0·48	0·47	0·46	0·47	0·50	0·59	0·70	0·57	0·62	0·64	0·38	0·43
Dy	2·90	2·84	2·81	2·92	2·63	2·90	3·20	2·57	2·55	2·47	2·57	2·39
Ho	0·67	0·57	0·59	0·57	0·49	0·45	0·49	0·41	0·34	0·30	0·56	0·51
Er	1·70	1·47	1·51	1·50	1·09	0·85	1·05	0·71	0·50	0·39	1·39	1·33
Tm	0·23	0·21	0·22	0·19	0·14	0·13	0·12	0·11	0·06	0·04	0·21	0·17
Yb	1·57	1·31	1·41	1·42	0·89	0·74	0·76	0·49	0·35	0·20	1·45	1·11
Lu	0·22	0·19	0·19	0·19	0·14	0·101	0·100	0·067	0·046	0·020	0·20	0·15
Hf	0·97	1·00	1·00	1·12	1·17	2·61	2·70	2·93	2·75	3·17	0·83	0·83
Pb	0·15	0·12	0·14	0·18	0·12	0·24	b.d.	0·14	0·15	0·13	0·40	0·45
Th	0·10	0·11	0·11	0·12	0·11	0·12	0·15	0·18	0·12	0·18	0·13	0·084
U	0·032	0·030	0·042	0·040	0·030	0·045	0·045	0·037	0·040	0·060	0·026	0·018
$(La/Pr)_n$	1·02	0·90	0·88	0·84	0·79	0·79	0·82	0·74	0·67	0·66	1·25	0·88
$(La/Yb)_n$	1·22	1·67	1·56	1·59	2·46	3·37	3·48	5·33	7·01	13·26	1·36	1·74
Sr/Sr*	1·04	0·89	0·88	0·83	0·79	0·68	0·71	0·65	0·65	0·65	1·35	1·06
Ti/Ti*	0·56	0·58	0·54	0·55	0·81	1·08	1·18	1·12	0·90	0·96	0·45	0·41
Zr/Zr*	0·64	0·55	0·57	0·54	0·59	0·72	0·73	0·68	0·65	0·63	0·70	0·57
Nb/Nb*	0·38	0·38	0·35	0·41	0·40	0·39	0·43	0·58	0·41	0·45	0·21	0·16

Incompatible trace elements

Clinopyroxenes of Cr-diopside suite xenoliths have uniform and low Ga contents (2·8–4·8 ppm) (Table 2, Fig. 4a), and those from composite xenoliths have higher Ga contents that increase significantly toward the pyroxenite portion with decreasing Mg-number (Fig. 4a). In contrast, Sr displays large variations in clinopyroxenes of different Cr-diopside suite xenoliths, but very limited variation within composite xenoliths despite the decrease in Mg-number from lherzolite to pyroxenite (Fig. 4b).

Ti in clinopyroxenes has the same pattern of variation as Ga, with low abundances and limited variation in the Cr-diopside suite xenoliths and high abundances and large variations in the composite xenoliths (Fig. 4c).

Table 2: continued

	transition zone megacryst			spinel lherzolite		gt pyroxenite		amp lherzolite	megacryst aggregate			
	Lz-17			Lz-37		Lz-37		Lz-29	Lz-29			
av.-no.	2	3	6	6	3	10	6	3	4	4	3	6
Mg-no.	73·9	72·1	56·8	85·2	83·2	79·7	77·8	79·4	73·7	68·8	65·7	61·8
Sc	32·9	7·5	6·3	45·3	36·4	25·4	20·2	32·6	14·0	11·0	7·7	7·6
Ti	4745	10388	10858	7694	8844	9332	8253	7140	8366	9000	10746	10912
V	197	245	254	230	251	265	308	201	188	189	215	227
Co	41·6	39·8	51·6	25·1	28·8	30·9	35·3	30·1	40·1	41·9	44·6	49·0
Ni	222	154	75·7	348	305	257	250	348	256	204	117	73·6
Zn	65·4	57·5	76·7	25·7	40·8	40·0	43·6	51·5	68·7	69·0	79·1	99·6
Ga	12·5	22·3	23·9	7·48	11·2	14·7	17·1	13·2	18·8	20·9	25·3	26·4
Sr	109	115	112	86·5	85·0	73·3	70·7	174	177	184	177	158
Y	9·35	8·61	7·50	14·7	13·3	12·7	10·7	13·6	9·90	9·04	9·53	9·77
Zr	41·2	68·2	70·4	60·3	63·8	68·5	56·0	98·6	87·6	90·5	106	99·8
Nb	0·25	0·51	0·50	1·75	1·50	2·12	1·90	0·91	0·81	0·77	0·84	0·79
Ba	1·01	b.d.	0·40	0·22	b.d.	0·20	0·30	0·30	0·50	0·35	b.d.	0·18
La	2·82	3·21	2·60	4·05	4·43	4·03	3·80	5·87	5·38	6·18	4·87	4·33
Ce	9·44	11·3	10·0	11·5	13·0	11·4	10·6	20·9	20·1	20·3	18·7	16·2
Pr	1·65	2·09	1·93	1·80	1·98	1·78	1·70	3·87	3·75	3·68	3·45	3·00
Nd	9·06	13·1	11·8	9·58	10·9	10·3	9·88	25·0	23·9	23·3	21·7	18·9
Sm	3·35	5·28	4·47	3·57	3·77	4·03	3·95	8·93	8·90	8·44	7·70	6·95
Eu	1·38	2·08	1·72	1·38	1·47	1·57	1·57	3·17	3·20	3·14	2·73	2·60
Gd	2·90	5·24	4·90	3·95	4·23	4·53	4·45	8·63	8·10	7·90	7·57	6·83
Tb	0·52	0·76	0·66	0·62	0·68	0·66	0·65	1·05	1·02	0·93	0·96	0·90
Dy	2·47	3·15	2·64	3·45	3·40	3·38	3·02	4·50	3·95	3·64	3·80	3·78
Ho	0·41	0·39	0·36	0·60	0·56	0·54	0·45	0·58	0·45	0·42	0·42	0·43
Er	0·87	0·55	0·44	1·39	1·16	1·00	0·81	1·06	0·56	0·55	0·64	0·61
Tm	0·08	0·05	0·05	0·18	0·15	0·12	0·08	0·10	0·06	0·05	0·04	0·04
Yb	0·56	0·25	0·14	1·07	0·82	0·66	0·42	0·68	0·31	0·16	0·17	0·18
Lu	0·063	0·030	b.d.	0·14	0·090	0·081	0·039	0·080	0·028	b.d.	0·019	0·023
Hf	1·28	2·91	2·98	2·15	2·80	2·67	2·02	4·13	3·53	3·15	4·30	4·05
Pb	b.d.	0·22	0·31	0·11	0·11	0·13	0·14	0·21	0·20	0·18	0·21	0·22
Th	0·071	0·065	0·035	0·14	0·14	0·16	0·17	0·13	0·11	0·098	0·075	0·049
U	0·023	0·019	0·023	0·033	0·030	0·040	0·038	0·033	0·029	0·021	0·021	0·019
$(La/Pr)_n$	0·65	0·58	0·51	0·86	0·85	0·86	0·85	0·58	0·54	0·64	0·53	0·55
$(La/Yb)_n$	3·46	9·02	12·74	2·61	3·74	4·23	6·23	5·94	12·19	26·48	19·41	16·65
Sr/Sr*	0·81	0·63	0·69	0·56	0·49	0·46	0·47	0·51	0·54	0·57	0·59	0·61
Ti/Ti*	0·55	0·74	0·89	0·78	0·84	0·83	0·74	0·32	0·39	0·43	0·56	0·61
Zr/Zr*	0·51	0·55	0·66	0·70	0·67	0·72	0·60	0·45	0·41	0·44	0·56	0·59
Nb/Nb*	0·14	0·26	0·29	0·67	0·54	0·78	0·74	0·26	0·25	0·22	0·29	0·31

$(La/Pr)_n$ and $(La/Yb)_n$, normalized to C1 chondrite (Anders & Grevesse, 1989). In the calculation of Sr/Sr*, Ti/Ti*, Zr/Zr* and Nb/Nb*, all elements are normalized to primitive mantle (McDonough & Sun, 1995), and Sr* = (Ce + Nd)/2, Ti* = (Eu + Gd)/2, Zr* = (Nd + Sm)/2 and Nb* = (U + La)/2. b.d., below the detection limit.

Nb, La and Ce are similar to Sr, with large variations in Cr-diopside suite xenoliths and slight variation in each composite xenolith (Fig. 4d and e). Clinopyroxenes in discrete Cr-diopside suite xenoliths have lower abundances of Sr, Nb, Zr, Ti and light REE (LREE) but higher Y and heavy REE (HREE) than those in both the Cr-diopside lherzolite and Al-augite pyroxenite domains of composite xenoliths (Fig. 4b–g). All REE in

Table 3: Trace-element compositions of amphiboles and garnets in Leizhou composite xenoliths (in ppm)

	amphibole							garnet			
	pyroxenite		lherzolite		lherzolite → pyroxenite			pyroxenite			
	Lz-10	Lz-20	Lz-21	Lz-29	Lz-37-1	Lz-37-2	Lz-37-3	Lz-10	Lz-17	Lz-29	Lz-37
av.-no.	3	5	5	2	3	5	5	6	3	9	3
Sc	15·8	13·1	23·6	21·2	27·7	22·4	14·3	32·9	11·7	20·8	47·4
Ti	37139	32757	26577	24073	22559	23585	21047	3393	3371	2360	1830
V	311	347	329	296	292	312	348	85·3	99·4	65·5	106
Co	40·3	49·2	43·7	76·2	44·5	49·3	56·3	46·2	76·3	61·6	59·0
Ni	522	626	634	1333	770	654	525	42·5	9·5	24·1	38·8
Zn	18·0	31·7	22·7	235	46·5	56·2	56·2	19·8	82·8	68·2	41·9
Ga	16·0	19·2	14·4	31·1	14·1	19·3	22·5	8·88	11·4	9·93	7·60
Rb	8·73	7·50	8·60	8·40	5·79	6·00	4·20	b.d.	b.d.	0·09	0·04
Sr	569	550	756	715	351	338	291	0·23	0·84	0·57	0·14
Y	10·5	10·5	11·0	13·1	13·8	12·9	11·0	63·4	66·5	68·7	47·3
Zr	42·7	56·1	60·4	76·7	42·6	45·2	40·2	58·0	45·6	48·8	30·0
Nb	32·4	32·7	21·4	39·7	57·7	60·2	60·6	0·08	b.d.	0·06	0·12
Ba	176	148	160	259	126	162	98·6	b.d.	b.d.	b.d.	b.d.
La	4·87	5·28	6·52	8·10	4·37	4·22	4·04	0·035	b.d.	0·22	0·030
Ce	12·9	14·4	16·1	26·7	11·8	11·8	10·7	0·15	0·56	0·77	0·11
Pr	2·17	2·28	2·36	4·75	1·81	1·8	1·72	0·064	0·15	0·21	0·04
Nd	12·7	13·7	12·9	30·4	10·5	10·4	10·2	0·84	2·34	2·67	0·63
Sm	4·60	4·84	3·64	9·65	3·67	3·76	3·92	1·31	3·12	3·60	1·02
Eu	1·77	1·76	1·54	3·55	1·52	1·55	1·62	1·00	2·13	2·31	0·81
Gd	4·73	4·82	3·68	8·75	4·13	4·26	4·36	5·94	9·27	10·5	3·80
Tb	0·61	0·67	0·53	1·11	0·65	0·63	0·64	1·70	2·10	2·37	0·98
Dy	2·83	2·96	2·52	4·35	3·30	3·32	2·98	12·7	15·0	15·4	8·03
Ho	0·42	0·43	0·46	0·55	0·57	0·53	0·48	2·52	2·84	2·79	1·86
Er	0·83	0·83	1·05	0·95	1·22	1·10	0·83	5·26	5·84	5·85	4·80
Tm	0·11	0·11	0·14	0·11	0·15	0·14	0·09	0·54	0·60	0·61	0·61
Yb	0·64	0·67	0·82	0·51	0·92	0·74	0·43	2·44	2·65	3·00	3·63
Lu	0·053	0·083	0·098	0·070	0·11	0·092	0·038	0·26	0·21	0·34	0·45
Hf	1·47	1·90	1·76	2·85	1·63	1·88	1·29	0·89	0·84	0·76	0·48
Pb	0·44	0·65	0·92	0·54	0·53	0·36	0·37	0·16	0·18	0·17	0·11
Th	0·11	0·18	0·36	0·13	0·10	0·11	0·12	0·022	b.d.	0·018	0·011
U	0·043	0·047	0·074	0·033	0·032	0·022	0·030	0·023	0·017	0·012	0·014

b.d., below the detection limit.

clinopyroxenes from Cr-diopside suite xenoliths decrease as Mg-number increases, whereas LREE and HREE in clinopyroxenes from Al-augite composite xenoliths exhibit different variation trends (Fig. 4 and inset in Fig. 4b and g).

Clinopyroxenes of the Cr-diopside suite xenoliths display different REE patterns with large $(La/Yb)_n$ variations (0·05–1·98), including LREE-depleted patterns (Fig. 5a) and LREE- to middle REE (MREE)-depleted patterns with LREE inflections (Fig. 5a and b). However, discrete Cr-diopside lherzolites Lz-2 and Lz-9 show remarkable LREE–MREE enrichment and relatively low HREE [$(La/Yb)_n > 1$] with a convex-upward shape pivot at Nd (Fig. 5a), although they have the same high Mg-number as the other discrete lherzolites. This enriched REE pattern is similar to that of some Al-augite composites (Fig. 5c–h), indicating that lherzolite Lz-2 and Lz-9 have been strongly metasomatized.

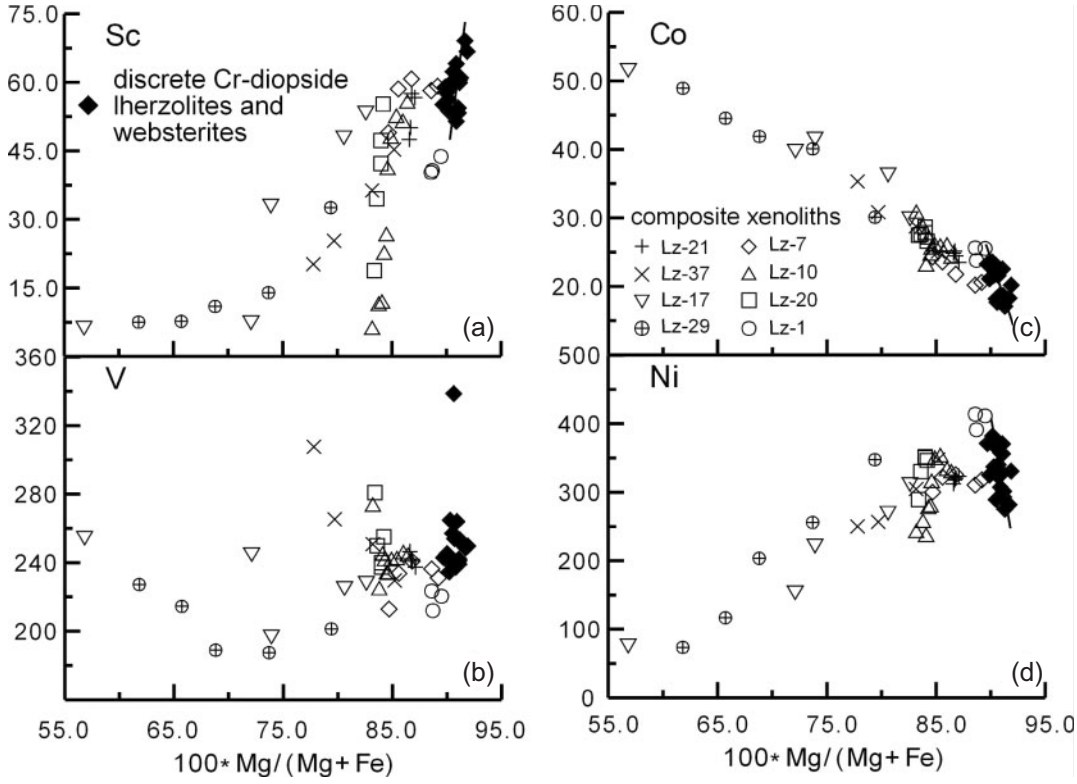

Fig. 2. Plots of Mg-number vs Sc, V, Co and Ni contents (in ppm) of clinopyroxenes from different xenolith types from the Leizhou Peninsula.

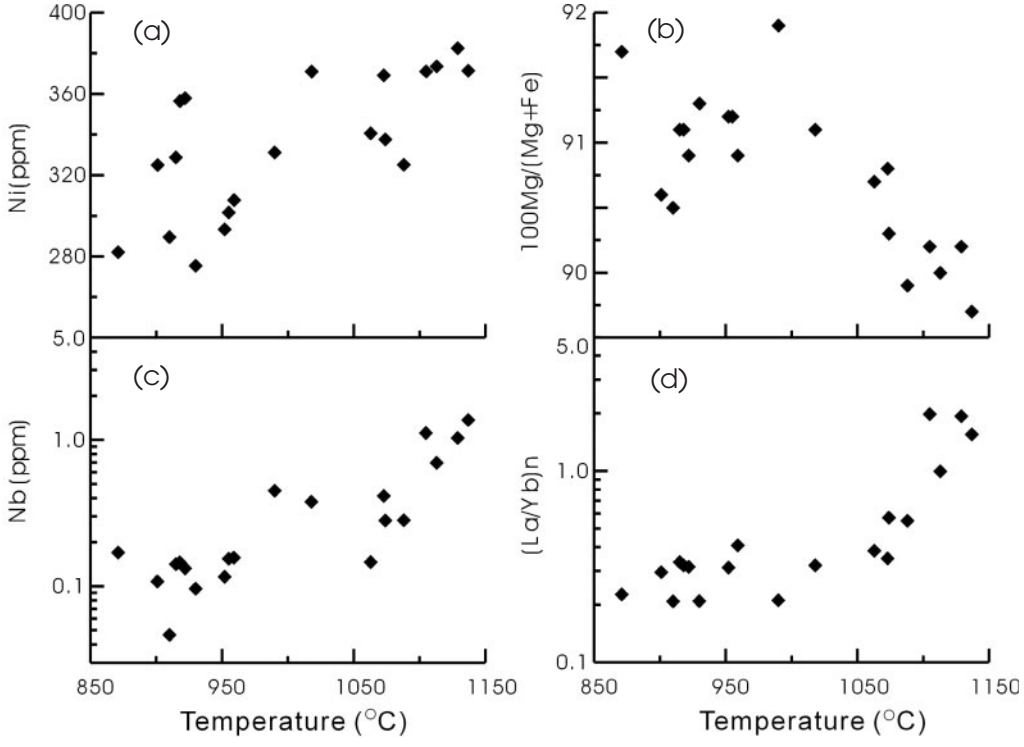

Fig. 3. Equilibrium temperature of Cr-diopside lherzolites vs Ni (a), Mg-number (b), Nb (c) and $(La/Yb)_n$ (d) of constituent clinopyroxenes from the Leizhou Peninsula. [See text for discussion of (b), (c) and (d).]

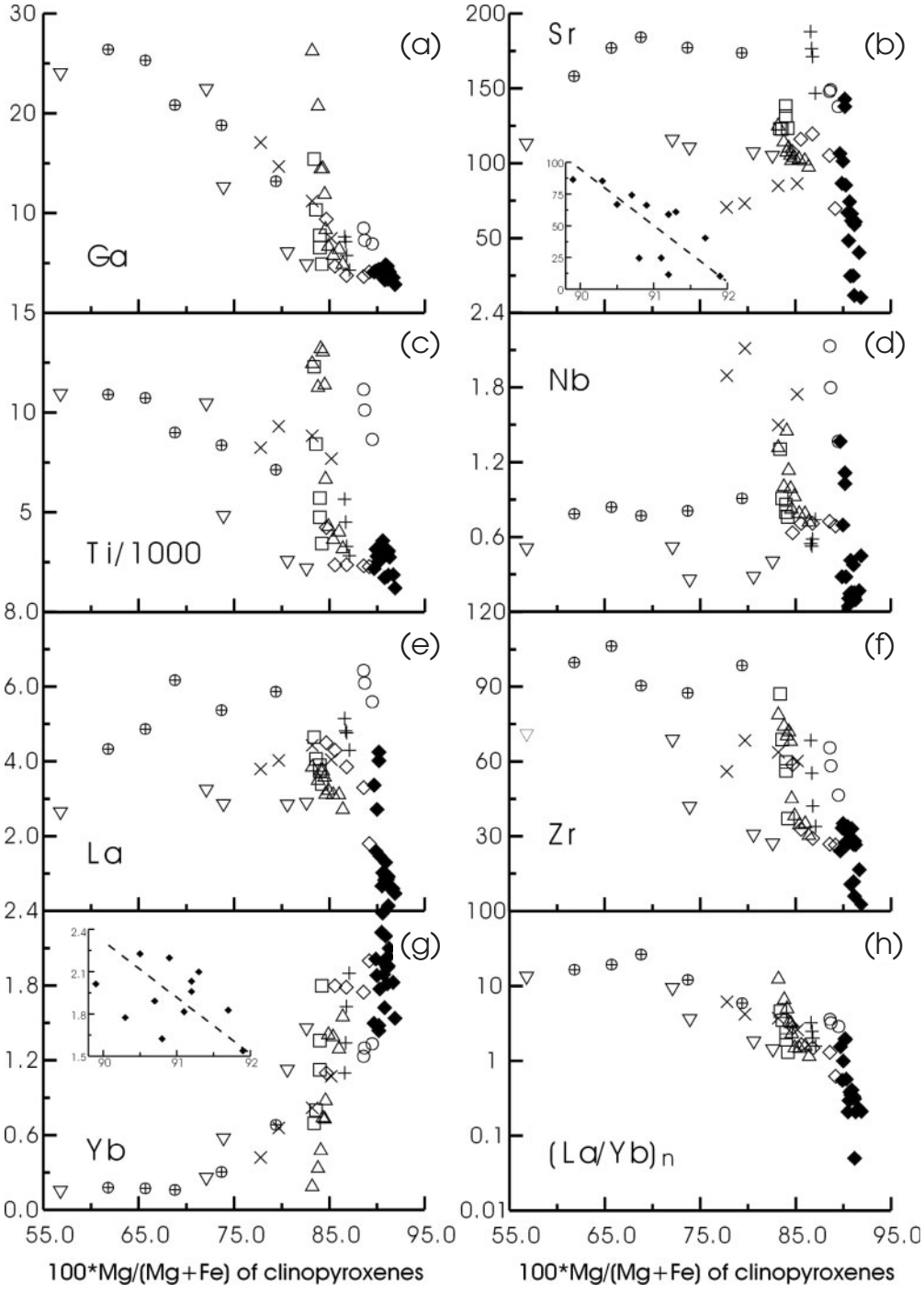

Fig. 4. Plots of Mg-number vs some incompatible elements (in ppm) of clinopyroxenes from different xenolith types from the Leizhou Peninsula. Insets in (b) and (g) are for Cr-diopside lherzolites only, and strongly metasomatized lherzolites are excluded. Symbols are as in Fig. 2.

All clinopyroxenes show a negative correlation of $(La/Yb)_n$ ratios with Mg-number (Fig. 4h) and some show a positive correlation with temperature (Fig. 3d).

Clinopyroxene REE patterns for Cr-diopside lherzolite parts of Al-augite composite xenoliths are distinct from those for discrete depleted Cr-diopside suite xenoliths, and more similar to metasomatized samples Lz-2 and Lz-9 (Fig. 5c–h). Clinopyroxene commonly displays large differences in REE patterns (Fig. 5c–f) from lherzolite to pyroxenite domains in composite xenoliths.

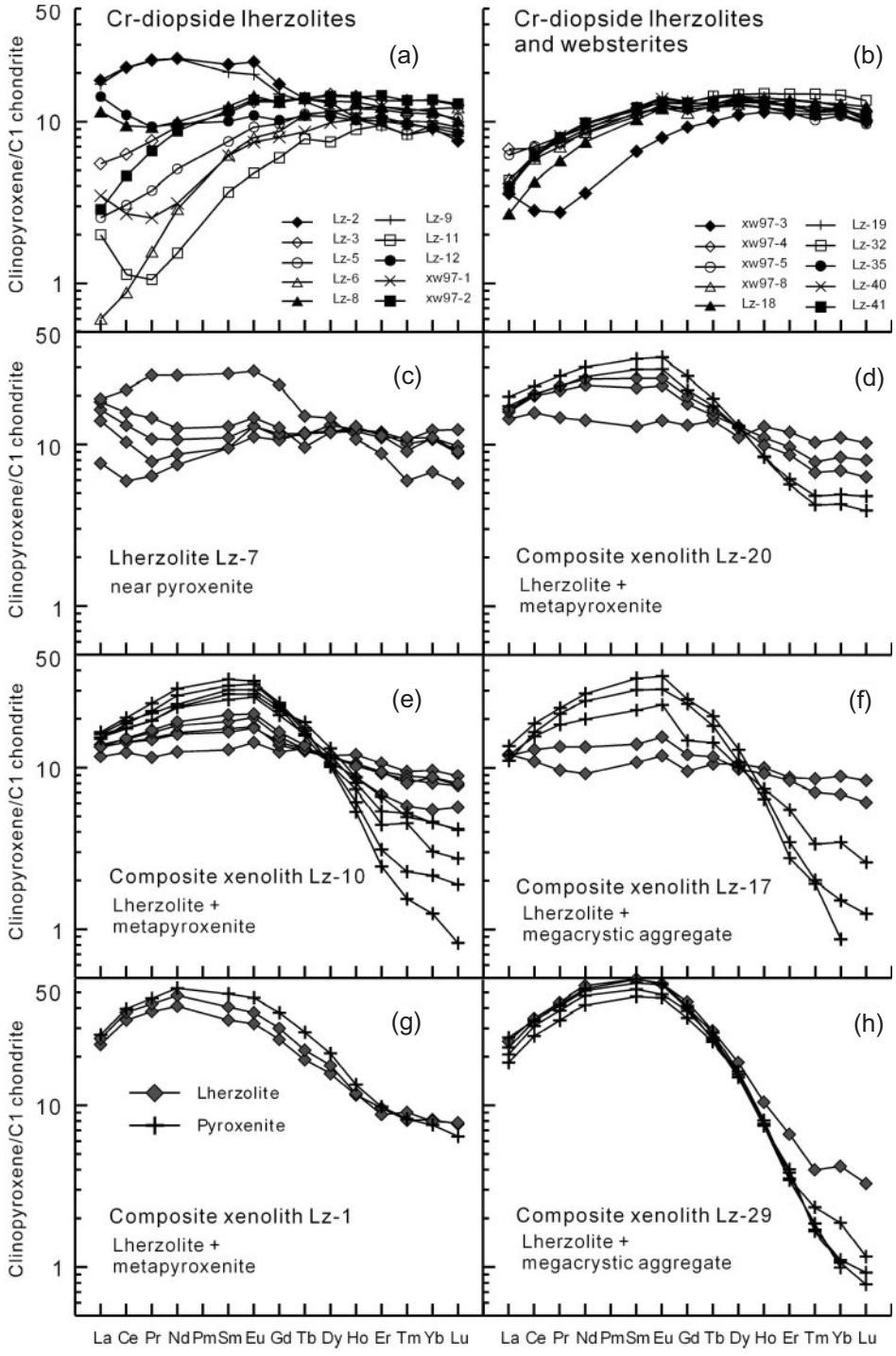

Fig. 5. REE patterns of clinopyroxenes in discrete Cr-diopside lherzolites and websterites (a, b), and Al-augite composite xenoliths (c–h) from the Leizhou Peninsula. Normalization factors for chondrite are from Anders & Grevesse (1989).

Clinopyroxenes in garnet-bearing pyroxenite of composites Lz-10, Lz-17, Lz-29 and Lz-37 have very low HREE abundances, probably as a result of HREE partitioning preferentially into garnet. However, those from garnet-free pyroxenites also have high LREE and low HREE relative to wall-rock lherzolite clinopyroxenes (e.g. composite xenolith Lz-20 and Lz-1), and clinopyroxenes from Cr-diopside domains in composite xenoliths have lower HREE contents than those from Cr-diopside suite lherzolites. This indicates that parental magmas of

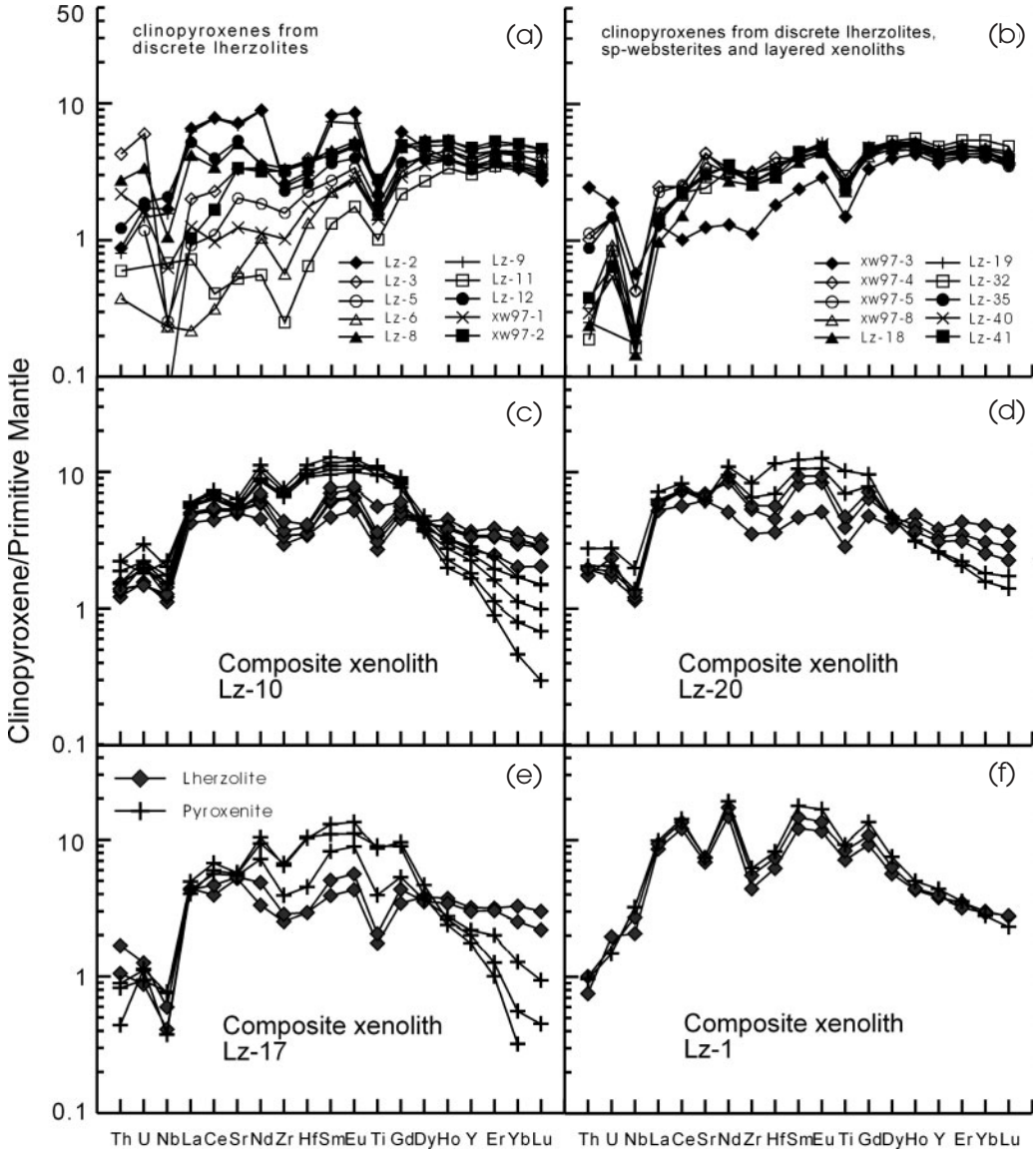

Fig. 6. Primitive mantle-normalized trace-element abundances of clinopyroxenes in different mantle xenoliths from the Leizhou Peninsula. Normalization factors for primitive mantle are from McDonough & Sun (1995).

the pyroxenites are more enriched in LREE and more depleted in HREE than an assumed melt in equilibrium with wall-rock lherzolite.

Most clinopyroxenes from Cr-diopside suite xenoliths have normalized trace-element patterns (Fig. 6) that show positive slopes from Th through Sr to MREE with significant negative anomalies in Nb, Zr and Ti (Fig. 6a and b), similar to those in fertile lherzolites from eastern Australia (O'Reilly & Griffin, 1988) and abyssal peridotites (Johnson *et al.*, 1990), but different from those in sp-lherzolites from Nushan and Niutoushan [more northerly localities in southeastern China (Xu *et al.*, 2000)]. Nushan sp-lherzolite clinopyroxenes (Group B) have lower HREE contents and higher concentrations of highly incompatible elements with weak Nb anomalies, similar to lherzolites Lz-2 and Lz-9 of this study (Fig. 6a). Niutoushan sp-lherzolite clinopyroxenes exhibit universally high incompatible element concentrations with stronger Nb negative anomalies (Xu *et al.*, 2000).

Incompatible-element abundance distributions of clinopyroxenes from Cr-diopside lherzolite domains of Al-augite composite xenoliths (including Lz-7 and Lz-21) are different from those of most Cr-diopside suite xenoliths (Fig. 6c–f). Composite xenolith clinopyroxenes often exhibit incompatible-element abundance distribution changes from the lherzolite to pyroxenite domains, especially in Sr, Zr and Ti anomalies. The

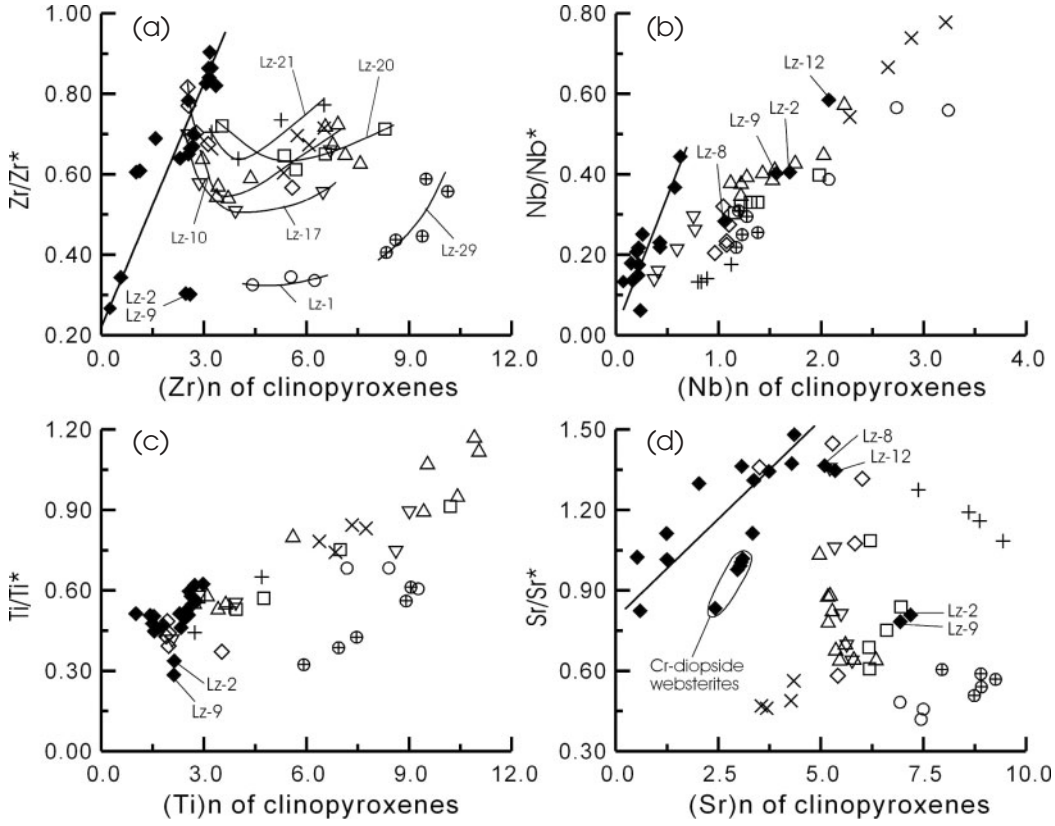

Fig. 7. (a) $(Zr)_n$ vs Zr/Zr*; (b) $(Nb)_n$ vs Nb/Nb*; (c) $(Ti)_n$ vs Ti/Ti* and (d) $(Sr)_n$ vs Sr/Sr* of clinopyroxenes from different xenolith types from the Leizhou Peninsula. The plots show different effects of partial melting and metasomatism on clinopyroxene compositions. All values were normalized to primitive mantle (McDonough & Sun, 1995). Zr* = (Nd + Sm)/2, Nb* = (U + La)/2, Ti* = (Eu + Gd)/2 and Sr* = (Ce + Nd)/2. Symbols are as in Fig. 2.

strength of Zr and Ti anomalies decreases from lherzolite to pyroxenite domains and the Sr anomaly changes from positive to negative (e.g. Ti in composite xenolith Lz-10, Lz-17 and Lz-20 and Sr in sample Lz-10 and Lz-17; Fig. 6c–e).

HFSE negative anomalies are very common in clinopyroxenes of mantle peridotites (Salters & Shimizu, 1988; Johnson *et al.*, 1990; Xu, *et al.*, 2000). Similar to the abyssal peridotites, clinopyroxenes of Cr-diopside suite xenoliths from the Leizhou Peninsula (except for Lz-2 and Lz-9) show increasingly negative Zr anomalies with decreasing Zr content of clinopyroxenes; that is, positive correlation of Zr/Zr* with $(Zr)_n$ (Fig. 7a). Clinopyroxenes in Al-augite composites and Lz-2 and Lz-9 all plot to the right of the Zr/Zr* vs $(Zr)_n$ correlation line for the Cr-diopside suite xenoliths, and show distinct differences in variation trend between lherzolite and pyroxenite. For example, the Zr content increases from lherzolite domain to pyroxenite in composite xenoliths Lz-10, Lz-17, Lz-20 and Lz-21, whereas the Zr/Zr* ratio decreases at first, and then increases (Fig. 7a).

Similarly, most clinopyroxenes of the Cr-diopside suite xenoliths show positive correlations between Nb/Nb* and Nb (Fig. 7b), but Lz-2, Lz-8, Lz-9 and Lz-12 deviate significantly from the correlation line with high Nb contents, possibly reflecting their metasomatic signature as indicated by their REE patterns (Fig. 5a). Clinopyroxenes of composite xenoliths have higher Nb and Nb/Nb*, and their Nb/Nb* values increase with Nb from lherzolite domain to pyroxenite domain (Fig. 7b). Ti/Ti* of clinopyroxenes in Cr-diopside suite xenoliths are low and show little variation (Fig. 7c), consistent with the observation of Johnson *et al.* (1990), whereas Ti/Ti* of clinopyroxenes from composite xenoliths are higher and increase with increasing Ti.

Sr/Sr* of clinopyroxene may be the best indicator of metasomatic intensity. Clinopyroxenes from most Cr-diopside suite xenoliths (Fig. 7d) have high Sr/Sr* ratios, low Sr contents and a positive correlation of Sr/Sr* with Sr, whereas those from Al-augite composite xenoliths and metasomatized lherzolite (e.g. Lz-2 and Lz-9) exhibit negative correlations between Sr/Sr* and Sr as well as a marked negative Sr anomaly (Sr/Sr* < 1, Fig. 7d). This indicates that LREE to MREE (i.e. Ce and Nd) increase more than Sr during the type of metasomatism that affected these rocks.

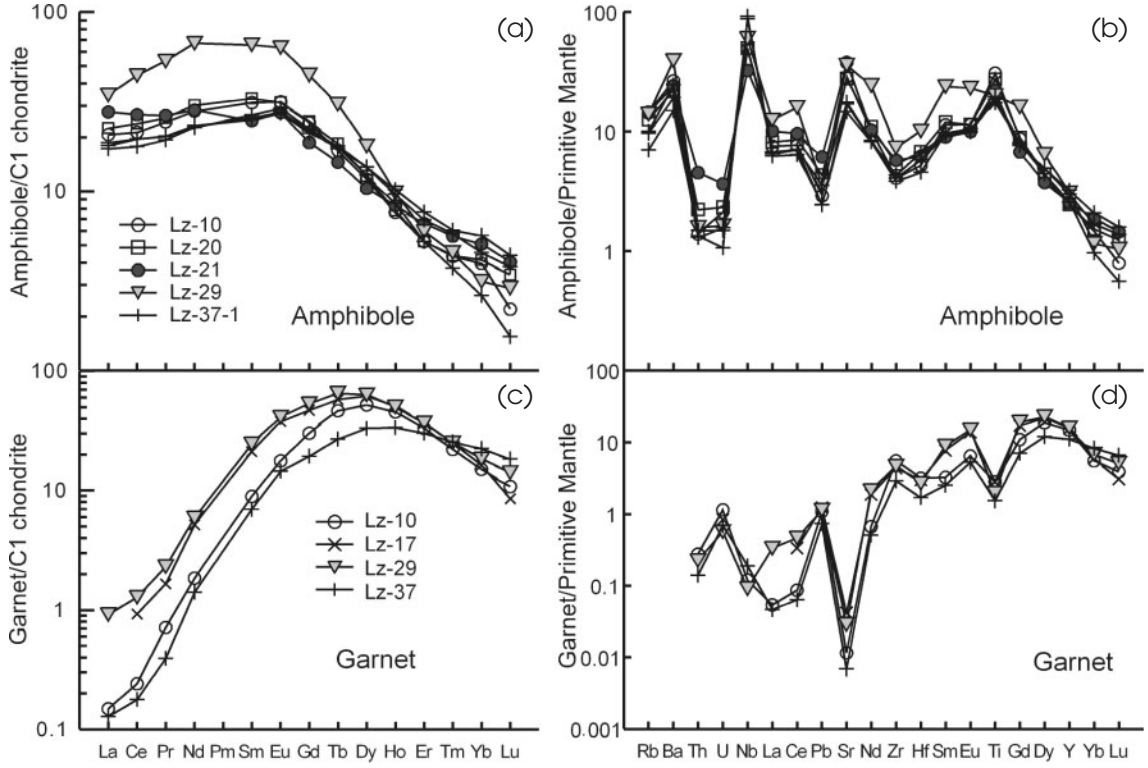

Fig. 8. (a) Chondrite-normalized REE patterns of amphiboles; (b) primitive mantle normalized incompatible element patterns of amphiboles; (c) chondrite-normalized REE patterns of garnets; (d) primitive mantle normalized incompatible element patterns of garnets in mantle xenoliths from the Leizhou Peninsula.

TRACE ELEMENTS IN AMPHIBOLE AND GARNET FROM COMPOSITE XENOLITHS

All analyzed amphiboles (Table 3) have REE patterns similar to those of the enriched clinopyroxenes (Fig. 8a). However, amphiboles have distinctive incompatible trace-element abundance patterns, with obvious Ba, Nb, Sr and Ti positive anomalies and Th, U, Pb, Zr and HREE negative anomalies (Fig. 8b), similar to those for Vitim xenoliths (Litasov *et al.*, 2000) and Lherz composite peridotite samples (Zanetti *et al.*, 1996), but different from those for Kerguelen xenoliths (Grégoire *et al.*, 2000). Amphibole from megacrystic composite xenolith Lz-29 has higher LREE and MREE than other samples and exhibits slightly different incompatible trace-element patterns with no positive Ti anomaly (Fig. 8a and b), indicating that these amphiboles were generated from melts with different compositions, analogous to amphibole origins for western Victorian (southeastern Australia) xenoliths (Powell *et al.*, 2004).

Garnet occurs only in the metapyroxenites of Al-augite composites Lz-10 and Lz-37 and in megacrystic aggregates of composite xenoliths Lz-17 and Lz-29. These latter garnets show much lower Mg-number (Table 1) and higher CaO content (7·07–7·67%) than garnets from metapyroxenites Lz-10 and Lz-37 (CaO 5·11–5·49%) (Yu *et al.*, 2003*a*). Compared with garnets in garnet peridotites from Nushan and Mingxi, southeastern China (Xu *et al.*, 2000) and Vitim, Russia (Ionov *et al.*, 1993), which have low LREE and high HREE patterns, Leizhou pyroxenite garnets have REE patterns with highest MREE and low LREE and HREE (Table 3; Fig. 8c) and their trace-element patterns have strong negative Sr and Ti anomalies (Fig. 8d). Garnets from megacrystic composites Lz-17 and Lz-29 show higher LREE and MREE and slightly lower HREE than those from metapyroxenite Lz-10 and Lz-37. Combined with their lower Mg-number, this suggests that the megacrystic aggregates have crystallized from a relatively more evolved magma than the metapyroxenites.

DISCUSSION

Partial melting origin for Leizhou depleted peridotites

Clinopyroxene is a major carrier of most trace elements and commonly has a similar incompatible-element pattern to its host peridotite (but 1–2 orders higher), except for lower Ba and Nb, and slight negative Ti anomalies (Chalot-Prat & Boullier, 1997; Zangana *et al.*, 1999;

Table 4: Depleted mantle source composition, partition coefficients and modes for modelling

	Source (ppm)	Partition coefficient of minerals/melt				D_i	P_i
		ol	opx	cpx	sp		
La	1·4	0·00004	0·0028	0·065	0·00002	0·012	0·045
Ce	4·63	0·00006	0·0032	0·09	0·00003	0·016	0·062
Nd	5·21	0·00031	0·0041	0·19	0·00004	0·034	0·130
Sm	2·05	0·00065	0·0058	0·3	0·00009	0·053	0·205
Eu	0·831	0·00075	0·0078	0·4	0·00014	0·071	0·274
Dy	3·83	0·0027	0·012	0·52	0·00021	0·093	0·356
Er	2·36	0·011	0·022	0·55	0·00033	0·106	0·380
Yb	2·2	0·027	0·039	0·58	0·00046	0·124	0·405
Lu	0·314	0·03	0·053	0·53	0·0008	0·121	0·374
Zr	39·4	0·001	0·021	0·16	0·06	0·035	0·114
Sr	80	0·00015	0·075	0·12	0·00003	0·042	0·097
Y	23	0·01	0·021	0·44	0·01	0·086	0·305
Source mode		51·6	29·2	17·0	2·2		
Melting mode		10	20	68	2		

Source clinopyroxene composition and starting mode are after Yang *et al*. (1998), except that Sr and Y contents of clinopyroxene in the source are based on this study; melting mode is after Johnson *et al*. (1990). Partition coefficients are those compiled by Yang *et al*. (1998); D_i and P_i are bulk partition coefficients of the starting depleted source and melting mode, respectively.

Grégoire *et al*., 2000; Xu *et al*., 2003). Accordingly, it has been used to effectively model the melting process and metasomatic enrichment in mantle peridotites (e.g. Johnson *et al*, 1990; Norman, 1998; Grégoire *et al*., 2000; Xu *et al*., 2000; Wang & Gasparik, 2001; Neumann *et al*., 2004).

Many clinopyroxenes of Leizhou Cr-diopside suite xenoliths are LREE-depleted (Fig. 5a and b), and their incompatible element contents and $(La/Yb)_n$, Zr/Zr* and Sr/Sr* ratios decrease with increasing Mg-number (Figs 4 and 7), suggesting variable degrees of melt extraction. The good positive correlation of incompatible trace elements and $(La/Yb)_n$ ratios with temperature (Fig. 3c and d) is consistent with the inference that the Leizhou upper mantle represents an earlier residual mantle column generated by decompression melting at different depths of an adiabatic upwelling asthenosphere (rather than a metasomatic event and/or mafic magma intrusions), analogous to mid-ocean ridge melting (McKenzie & Bickle, 1988; Yang *et al*., 1998). Therefore, the trace-element contents of clinopyroxenes from the depleted lherzolites in this study may provide clues about the geodynamic history of the lithospheric mantle beneath the Leizhou Peninsula, South China.

So far three melting models, batch, fractional and incremental melting, have been used to fit the composition variation of the mantle peridotites (e.g. Johnson *et al*., 1990; Norman, 1998; Yang *et al*., 1998; Xu *et al*., 2000). Fractional melting depletes the residue in incompatible elements far more effectively than batch melting does and the two processes are easily distinguished in REE diagrams and plots of incompatible elements in the residues (Johnson *et al*., 1990; Norman, 1998). Incremental melting is intermediate to batch and fractional melting. In this study all three melting models have been tested to choose the best for explaining compositional variation observed in Leizhou lherzolites.

Melting style and extents were modelled using REE, Y, Zr, and Sr concentrations in clinopyroxenes in this study. The equations are those given by Johnson *et al*. (1990). The input parameters needed in these models are starting source composition, partition coefficients, and proportions of minerals in the source and those contributing to the liquid. The model starting composition was inferred to be a residue after removing 1–3% melt generated by batch melting from the primitive mantle (Hart & Zindler, 1986; Johnson *et al*., 1990; Hirschmann & Stolper, 1996; Yang *et al*., 1998) which these workers preferred, based on mass balance and $^{143}Nd/^{144}Nd$ and $^{177}Hf/^{176}Hf$ ratios. The present study accepts such depleted peridotite after 2% melt removal as the source composition. The mineral proportions of this slightly depleted source and those phases entering the melt are taken from Yang *et al*. (1998) and Johnson *et al*. (1990), respectively, and partition coefficients for different minerals are from published data (Table 4).

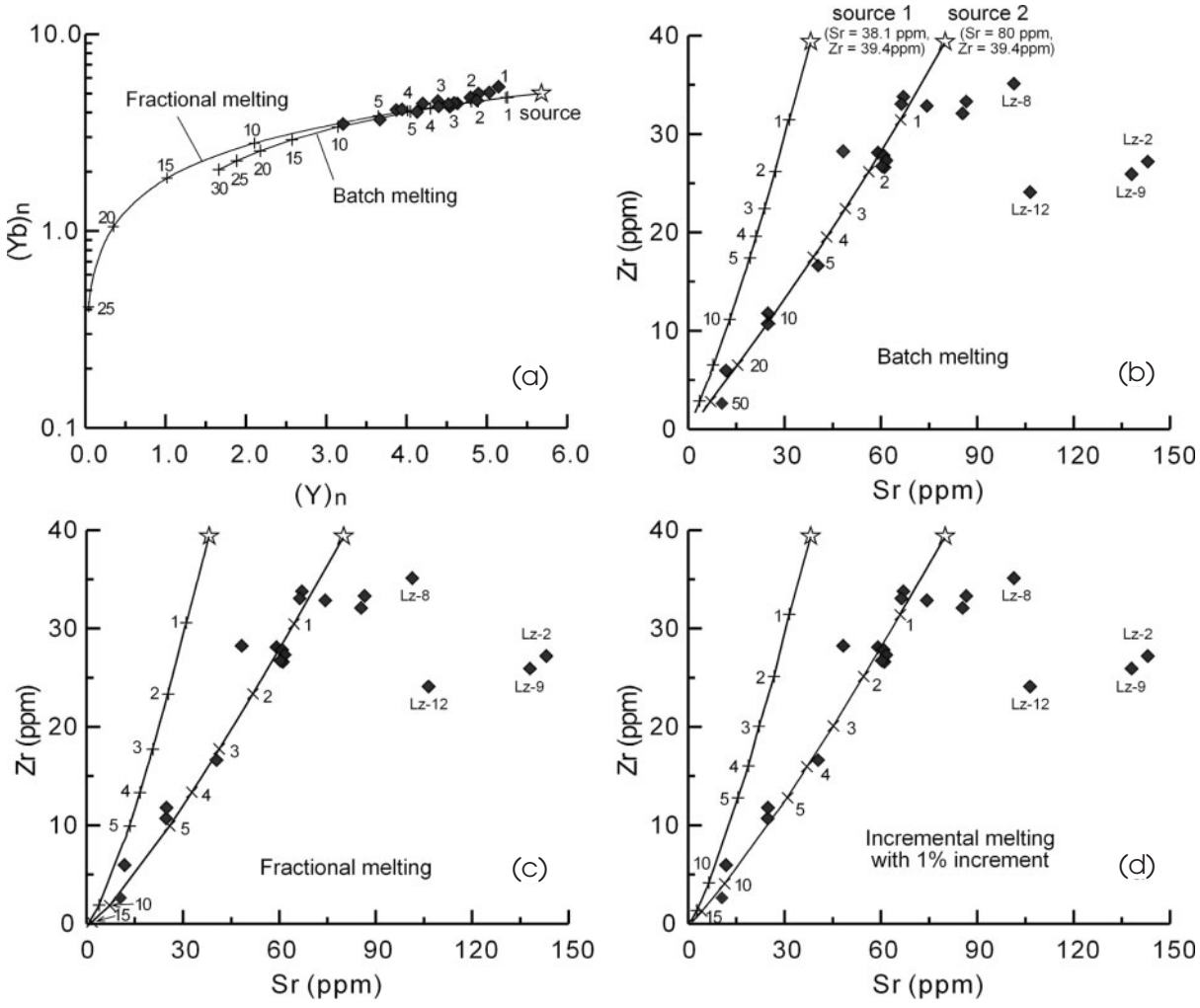

Fig. 9. (a) Batch and fractional melting models of Y and Yb contents for mantle clinopyroxenes from Leizhou xenoliths; (b) batch melting, (c) fractional melting; (d) incremental melting models of Sr and Zr contents for clinopyroxenes in discrete Cr-diopside lherzolites from the Leizhou Peninsula. (See text for further explanation.)

Y and Yb modelling

Y and Yb concentrations of clinopyroxenes were used by Norman (1998) and Xu *et al.* (2000) to model the partial melting process, because of their low mobility relative to LREE. However, our data show that metasomatism can result in not only enrichment in LREE and large ion lithophile elements (LILE) but also at least relative depletion in HREE and Y in the Cr-diopside lherzolite xenoliths (Figs 4 and 5), especially in strongly metasomatized ones. The same observations have been reported in other metasomatized samples worldwide, e.g. Shadwell peridotites, southeastern Australia (Norman, 1998), Dariganga peridotites of Mongolia (Wiechert *et al.*, 1997) and clinopyroxene inclusions in diamonds from Liaoning, North China (Wang & Gasparik, 2001). Thus modelling based on Y and Yb concentrations of metasomatized clinopyroxenes may lead to overestimation of the extent of partial melting. Therefore melt modelling was carried out only for LREE-depleted clinopyroxenes to avoid such ambiguity.

Modelling results show that Y and Yb contents of clinopyroxenes from Leizhou lherzolites can be reproduced by both batch and fractional melting with reasonable degrees of melting (Fig. 9a). Only 1–7% fractional melting is necessary to generate Y and Yb contents observed in these lherzolite clinopyroxenes, and about 10% melt needs to be removed in batch melting model to form the most depleted lherzolite Lz-11. Evidently, Y and Yb concentrations are insensitive to melting styles for the lherzolites with low degrees of melting.

Zr and Sr modelling

Zr and Sr concentrations of clinopyroxenes were used by Yang *et al.* (1998) to model melting processes, because

they may more effectively distinguish batch melting from fractional melting models. However, Sr is affected easily by metasomatism, so possible metasomatic effects must be ruled out before modelling. The Zr–Sr plots of Cr-diopside suite xenoliths (Fig. 9b–d) show that depleted and slightly metasomatized clinopyroxenes result in a consistent correlation whereas more strongly metasomatized samples, such as Lz-2, Lz-9, Lz-12 and Lz-8, deviate significantly and are more enriched in Sr at given Zr levels.

Melting trends based upon three models (batch, fractional and incremental melting) are shown in Fig. 9b–d. The compositional variations for Zr and Sr in the Leizhou Cr-diopside wall-rock xenoliths can be successfully modelled using a Sr content of 80 ppm for the source (source 2 of Fig. 9b–d), rather than the 38·1 ppm used in the modelling of Yang *et al.* (1998) (source 1 of Fig. 9b–d).

Although all three models (batch, fractional and incremental) reproduce the natural trends in Sr and Zr of the clinopyroxenes, different melting degrees are required for each melting style. To reproduce Zr and Sr contents of the most depleted sample Lz-11, an unrealistic 50% batch melting would be required (Fig. 9b). In contrast, fractional melting and incremental melting can both produce residual peridotite with the Sr and Zr values of Lz-11 with reasonable degrees of melting of about 9% (Fig. 9c) and 12% (Fig. 9d), respectively. However, this Zr and Sr modelling method cannot further discriminate effectively between these two melting styles.

REE modelling

Total REE patterns in peridotite clinopyroxenes provide important constraints to test melting models for unmetasomatized mantle peridotites (Johnson *et al.*, 1990; Yang *et al.*, 1998). All three melt models generate REE patterns that are consistent with the observed REE abundances in lightly depleted Cr-diopside wall-rock xenoliths from the Leizhou Peninsula (Fig. 10). However, batch melting does not yield matching patterns for REE for the highly depleted clinopyroxenes (Fig. 10a), for example, as 20% batch melting generates a pattern with higher LREE and lower HREE than the natural samples (e.g. Lz-11).

Fractional melting produces a matching REE pattern for the slightly depleted lherzolite at 4% melting (Fig. 10b), but more than 5% fractional melting more rapidly depletes the LREE relative to HREE, inconsistent with the observed clinopyroxene patterns for the Leizhou highly depleted lherzolites (Fig. 10b). Incremental melting with 2% increments best fits the REE characteristics of all Leizhou lherzolite clinopyroxenes, and Fig. 10c illustrates that the range of Leizhou lherzolites may be generated by from about to (1 to 10%) incremental melting (at increments of 1–2%) of a depleted mantle source.

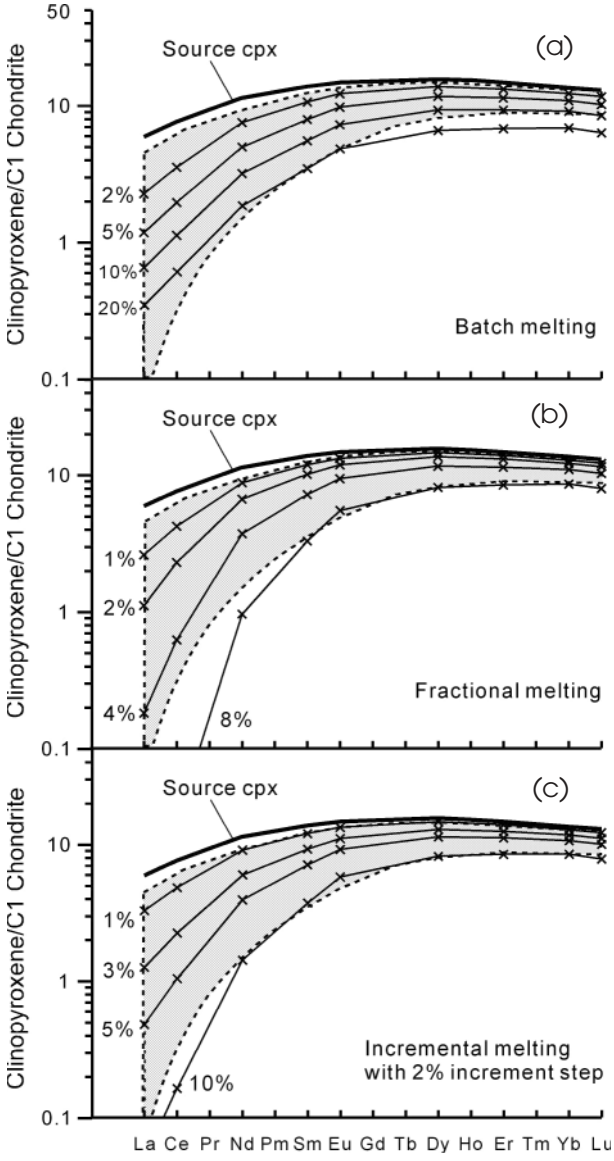

Fig. 10. Modelling of REE patterns for clinopyroxenes from Leizhou Cr-diopside lherzolites. (a) Batch melting, LREE depletion in residual clinopyroxene being less effective than HREE depletion. (b) Fractional melting, generally yielding too strong LREE depletion relative to HREE. (c) Incremental melting of 1–10% with 2% increment, providing good agreement with clinopyroxenes from Leizhou Cr-diopside lherzolites. Diagonal fields are compositional ranges of LREE-depleted clinopyroxenes from the Leizhou lherzolites (Fig. 5a). Lowest La and Ce contents are extrapolated based on the most depleted clinopyroxenes (Lz-11) after eliminating post-melting metasomatic enrichment in La and Ce.

Geodynamic considerations of melt modelling results

Incremental melt models have been shown to be the best matches for the geochemical parameters of the natural samples from the Leizhou lithospheric mantle and this

can be reconciled with geodynamic processes relevant to its formation.

Johnson *et al.* (1990) suggested that the compositional variations observed in abyssal peridotites, inferred to be the residues of partial melting processes that produce MORB, reflect a process of melt extraction that involves the removal of small increments of melt (about 0·1% increment). Yang *et al.* (1998) considered that a 1% incremental batch melting model yields the best fit to the REE, Sr and Zr abundances in clinopyroxenes from Hawaiian lherzolites. Experimental studies and theoretical calculations also indicate that mantle melting beneath mid-ocean ridge environments favours a near fractional melting process rather than pure fractional melting and batch melting (McKenzie, 1984; Riley & Kohlstedt, 1991; Langmuir *et al.*, 1992; Iwamori *et al.*, 1995). Perfect fractional melting is dynamically more difficult for large mantle melt columns or domains because of the difficulty in segregating sufficient melt volumes, and the mantle wall-rock xenoliths in this study have been shown (by the large temperature range) to represent samples from a large vertical section (~30 km). Upwelling asthenospheric mantle such as occurs during lithosphere extension or other convective upwelling would be characterized by this type of incremental melt column segregation process, similar to that described by McKenzie & Bickle (1988). A higher incremental melting fraction (1–2%) for Leizhou xenolithic lherzolites than that of abyssal peridotites (0·1%, Johnson *et al.*, 1990) probably reflects the difference in the mantle upwelling rate. Smaller incremental step-melting may correspond to conditions of fast upwelling and strong extension (e.g. Pacific mid-oceanic ridge), whereas larger incremental step-melting was limited for conditions of slow extension and low rates of asthenosphere upwelling (e.g. rifting near a continental margin; Leizhou, this study).

Melt production rate (d*F*/d*P*) and mafic lower crustal thickness in the Leizhou lithosphere

Melt production rate is the ratio of the difference between the highest and lowest degrees of melting (d*F*) to the difference in their equilibrium pressures (d*P*) in a residual mantle column (Langmuir *et al.*, 1992; Yang *et al.*, 1998). The melt modelling calculations above indicate that the highest and lowest melt fractions are 10–12% and 1% respectively for the Leizhou lithospheric mantle observed at present, and thus (d*F*) is about 10%. Figure 3c and d shows that incompatible element concentration is positively correlated with temperature, suggesting that the melting degrees of lherzolites decreased with increasing temperature (proxy for depth). As there are no robust methods for geobarometry for spinel lherzolites, the pressures of Leizhou lherzolites are estimated referring calculated temperatures (Brey & Köhler, 1990, two-pyroxene thermometer) to the well-constrained xenolith-derived geotherm (Yu *et al.*, 2003*a*). The temperature range of the sampled mantle wall-rock lherzolites (except for four highly metasomatized lherzolites) is from 870°C to 1090°C (Table 1), corresponding to pressures of 9 and 18 kbar respectively and a depth range of about 30–60 km. This results in an estimated linear mean melt production rate of about 1·1%/kbar for the Leizhou lithospheric mantle over its 30 km depth range.

This melt production rate is similar to the estimations (1·2–1·3%/kbar) for the oceanic mantle beneath mid-ocean ridges (Langmuir *et al.*, 1992; Iwamori *et al.*, 1995; Shen & Forsyth, 1995). It is therefore suggested that Leizhou lithosphere mantle was formed in a strong extensional setting, probably related to Mesozoic lithospheric thinning of South China (Xu *et al.*, 2000), and represents an upwelling asthenospheric melting column that cooled to become new lithospheric mantle.

The extent of crustal growth as a result of intrusion of mafic melts near the crust–mantle boundary from such a melting event can be calculated to be about 5–6 km according to the melt production rate and the formula proposed by Forsyth (1993), and previously had been modelled for a similar tectonic environment in eastern Australia by Cull *et al.* (1991).

Seismic surveys show that the crustal thickness of the studied area is about 28 km and that the lower crust velocities are consistent with mafic granulites from about 20 km to 28 km (Lin *et al.*, 1988). In addition, Yu *et al.* (2003*a*, *c*) used xenolith suites to demonstrate that the lower crust in this region is indeed composed of mafic granulites and cumulates. These observations and the calculation of the thickness of basaltic addition from the inferred degrees of partial melting suggest that the lower crust beneath the Leizhou Peninsula was probably generated by underplating during the formation of new lithospheric mantle by cooling of a column of upwelling asthenosphere that had undergone differential and gradational partial melting over its vertical extent.

Metasomatic modification of the Leizhou lithospheric mantle

Metasomatic effects

Almost all discrete lherzolites from the Leizhou Peninsula lack modal metasomatic phases, but show a wide range of modes and geochemical compositions, reflecting significant vertical mantle heterogeneities. The melting calculations detailed above explain trace-element variations of depleted lherzolites as due to different degrees of depletion. However, all the enriched lherzolites, including those in composite xenoliths, have geochemical signatures (Figs 4–7) that cannot be interpreted by melt

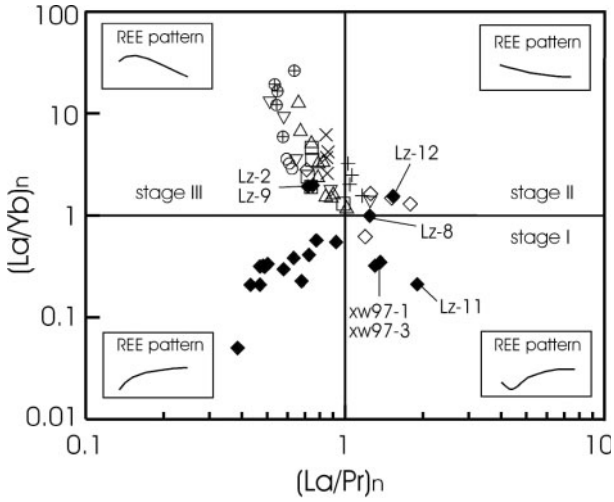

Fig. 11. $(La/Pr)_n$ vs $(La/Yb)_n$ of clinopyroxenes from different xenolith types from the Leizhou Peninsula, reflecting variable effects of metasomatism. Symbols are as in Fig. 2.

depletion processes and reflect subsequent metasomatic events.

The similarity in clinopyroxene REE patterns in both Cr-diopside lherzolites and Al-augite pyroxenites juxtaposed in some composite xenoliths (e.g. Lz-1 and Lz-29; Fig. 5g and h) suggests that lherzolites were strongly metasomatized by mafic melts parental to the intruding Al-augite rock types (or that both rock types were metasomatized by a similar agent).

However, Cr-diopside lherzolites in other composite xenoliths (Lz-10, Lz-17 and Lz-7) have clinopyroxene REE patterns distinct from those of the pyroxenites, with lower $(La/Yb)_n$ and higher $(La/Pr)_n$ (Figs 5c–f and 11). The extent of metasomatism (or enrichment) decreases distinctly with distance from the contact and the sequence of changing REE pattern is typical of chromatographic changes in percolation processes (Navon & Stolper, 1987; O'Reilly & Griffin, 1988; O'Reilly *et al.*, 1991).

Clinopyroxenes from discrete lherzolites Lz-2 and Lz-9 show strong cryptic metasomatism (Figs 5a, 6a and 11) with enrichment in LREE, Sr and Nb, and relative depletion in Y and HREE. Moderately metasomatized Cr-diopside lherzolites (e.g. Lz-8 and Lz-12) have clinopyroxene REE patterns with $(La/Yb)_n \geq 1$ and $(La/Pr)_n > 1$ (Figs 5a and 11). In this metasomatic type, most of the highly incompatible elements are moderately enriched, and Y and HREE weakly depleted.

Clinopyroxenes from weakly metasomatized lherzolites are slightly enriched in La, Ce, Sr and Nb compared with the depleted ones, but still have $(La/Yb)_n < 1$ with an upward inflection at La and Ce with $(La/Pr)_n > 1$ (e.g. Lz-11, xw97-1 and Lz-7).

Good discrimination of different metasomatic types can be shown in plots of $(La/Yb)_n$ vs $(La/Pr)_n$ (Fig. 11), similar to the plots used by Xu *et al.* (2000), which distinguish different types of REE patterns. Original depleted lherzolite clinopyroxenes plot in the lower-left field of this plot, and highly enriched clinopyroxenes from lherzolites and pyroxenites are in the upper-left field. Weakly metasomatized samples plot in the lower-right quadrant, and moderately metasomatized ones in the upper-right quadrant.

Nature of metasomatic agents

Differences in clinopyroxene compositions between enriched discrete lherzolite and composite lherzolite document distinct metasomatic agents and variations in the degree of metasomatism. Previous studies have demonstrated various metasomatic agents occurring in mantle peridotites, including carbonatitic melts (e.g. Baker *et al.*, 1998; Yaxley *et al.*, 1998; Gorring & Kay, 2000; Wang & Gasparik, 2001), siliceous melts (e.g. Menzies *et al.*, 1987; Vannucci *et al.*, 1998; Zangana *et al.*, 1999; Grégoire *et al.*, 2000), adakitic (Kepezhinskas *et al.*, 1995, 1996; Schiano *et al.*, 1995), melilitic or melanephelinitic melts (Chalot-Prat & Boullier, 1997) and fluids (CO_2-, H_2O-, halogen- or P-rich) (O'Reilly & Griffin, 1988; Baker *et al.*, 1998; Gorring & Kay, 2000; Larsen *et al.*, 2003). These metasomatic agents may give rise to distinct chemical variations for the mantle peridotites but may be difficult to distinguish using lherzolitic clinopyroxene compositions alone (Vannucci *et al.*, 1998).

Composite xenoliths

The compositions of clinopyroxenes vary sequentially from Cr-diopside lherzolites to juxtaposed pyroxenites in the composite xenoliths (Figs 4–6), and thus it is inferred that the lherzolites were metasomatized by the siliceous melts or fluids released from them that formed the pyroxenites. These clinopyroxenes are relatively low in MgO, very low in HREE, Y, Sc and Ni, and enriched in LREE–MREE (La to Gd), Sr, Nb, Zr, Hf, Ti, Ga and Co (Figs 2 and 4) compared with clinopyroxenes in the depleted discrete Cr-diopside lherzolites. Because of the strong compositional gradients observed in the lherzolites in contact with pyroxenites, it is generally not possible to simply calculate the composition of the original metasomatic agent using partition coefficients and enriched lherzolitic clinopyroxenes. However, the composition of the pyroxenites most distant from the contact zone may directly reflect the chemical features of their parental magma, and this magma may represent the original metasomatic agent. In addition, amphibole compositions in pyroxenite and lherzolite near pyroxenite also may reflect chemical fingerprints of the metasomatic agent (Bodinier *et al.*, 2004).

The parental magmas of pyroxenites in composite xenoliths have been calculated using the clinopyroxene

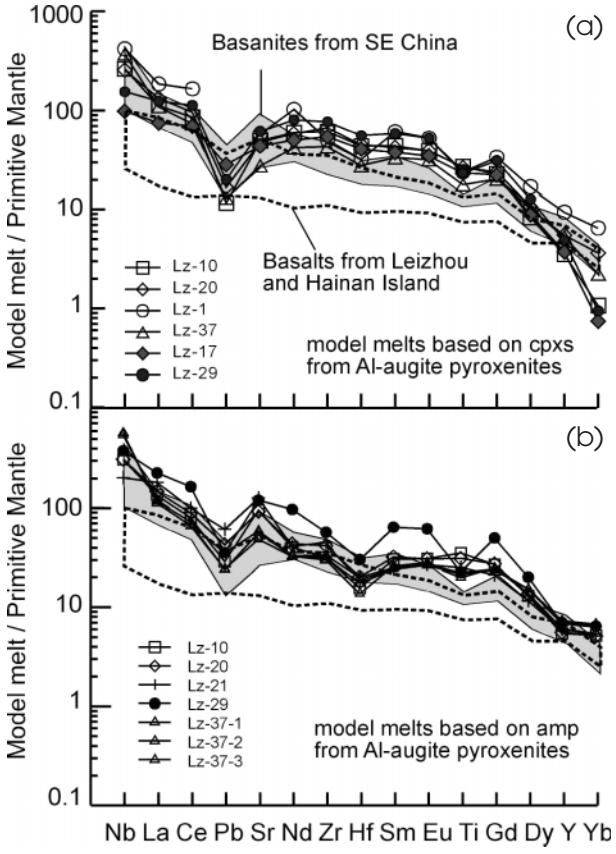

Fig. 12. Primitive mantle normalized incompatible trace-element patterns of the model melts in equilibrium with the clinopyroxenes from pyroxenites most distant from the contact zone in composite xenoliths (a) and in equilibrium with amphiboles from pyroxenite and lherzolites proximal to the contact (b). The clinopyroxene/melt partition coefficients are from Hart & Dunn (1993), and amphibole/melt partition coefficients from McKenzie & O'Nions (1991), Adam & Green (1994) and La Tourrette *et al.* (1995); the compositional range of basanites in southeastern China is from Zou *et al.* (2000), and that of Cenozoic basalts in Leizhou and Hainan Island from Flower *et al.* (1992) and Liu *et al.* (1994).

compositions and the partition coefficients of Hart & Dunn (1993). The metasomatic melts in equilibrium with amphiboles were calculated using the partition coefficients of McKenzie & O'Nions (1991), Adam & Green (1994) and La Tourrette *et al.* (1995). The calculation results show that the melts deduced from clinopyroxene and amphibole have similar compositions (Fig. 12), consistent with the observation of Bodinier *et al.* (2004), suggesting the clinopyroxenes have re-equilibrated with the metasomatic melt. These calculated melts have very high incompatible element abundances with obvious Pb and slight Ti negative anomalies (Fig. 12). These trace-element signatures resemble those of basanites from Nushan, Xilong and Mingxi, southeastern China (Zou *et al.*, 2000) with slightly higher contents of moderately incompatible elements (from Zr to Gd), but differ from those of basalts from the Leizhou Peninsula and Hainan Island (Flower *et al.*, 1992; Liu *et al.*, 1994) that have much lower contents of most incompatible elements. This indicates that these pyroxenites, especially the metapyroxenites, are not high-pressure products of the host basalt or the basalts widespread in the study area, implying that the metasomatism event occurred before host magmatism (6–0·3 Ma) and possibly took place during the SCSB opening (or earlier). Megacrystic aggregates Lz-17 and Lz-29 show igneous microstructures and different geochemical characteristics [much lower Mg-number and higher $(La/Yb)_n$] than the metapyroxenites. Geochemical modelling for clinopyroxene and garnet megacrysts indicates that these megacrysts crystallized from a highly evolved magma consistent with derivation by 70–80% fractional crystallization of a quartz tholeiite similar to those in the Leizhou and Hainan area (Yu & O'Reilly, 2001; Yu *et al.*, 2003*b*). This observation suggests that they were formed recently (probably related to early post-spreading magmatism) and represent a different episode of metasomatism in Leizhou mantle.

The absence of negative Nb, Zr and Hf anomalies and the marked negative Pb anomaly exclude subduction-related processes or the involvement of a crustal component in the melt source. The low La/Nb, K/U, Ba/Nb and Zr/Nb ratios and high Ce/Pb and Zr/Hf ratios (Table 5) of these calculated compositions closely resemble HIMU-type OIBs, suggesting a possible HIMU component in the source. Possibilities for the source origin include a plume with a HIMU signature or an upwelling asthenosphere with these characteristics. It is relevant to note that there is present-day geophysical evidence for a plume in this region (Lebedev & Nolet, 2003). This metasomatic event caused by the upwelling of a plume or asthenosphere overprinted the mantle lithospheric column that had previously formed as described above.

Enriched discrete lherzolites

Discrete enriched Cr-diopside lherzolites (e.g. samples Lz-2 and Lz-9) have geochemical signatures (including high Sr and LREE and relatively low HFSE abundances) characteristic of those inferred to derive from the metasomatic effects of carbonatitic melts or CO_2-rich fluids (e.g. Sun & Kerrich, 1995; Wiechert *et al.*, 1997; Baker *et al.*, 1998; Gorring & Kay, 2000; Wang & Gasparik, 2001). However, these clinopyroxenes have relatively low Mg-number (89·7–90·2) and CaO (18·8–19·0 wt %) and high Al_2O_3 (6·53–6·89 wt %) and TiO_2 (0·37–0·51%) contents (Yu *et al.*, 2003*a*), inconsistent with carbonatitic melt metasomatism (Coltorti *et al.*, 1999; Wang & Gasparik, 2001). Also, they do not plot in the field for carbonatitic metasomatism in the discriminative diagram of La/Yb vs Ti/Eu proposed by Coltorti *et al.* (1999). On the other hand, these clinopyroxenes have much higher Sr, LREE and Mg-number and lower Ti, Zr and Hf than

Table 5: Comparisons of characteristic incompatible element ratios of calculated parent melts for Leizhou pyroxenites with typical basalts from different mantle sources

	Lz-10	Lz-20	Lz-1	Lz-37	Lz-17	Lz-29	HIMU-1	HIMU-2	MORB	EM-I	EM-II	OIB
K/Nb	50	23	23	21	117	169	116	80–160	250–440	324	308	250
K/U	1477	724	2177	1408	3398	9627	5840	4000–8000	>12000			11800
Ba/Nb			1·4	1·8	9·2	2·5	4·3	4·5–5·3	2·7–11·7	8·4	10·3	7·3
Th/Nb	0·085	0·108	0·023	0·056	0·045	0·040	0·073	0·06–0·08	0·050	0·10	0·13	0·083
La/Nb	0·42	0·51	0·43	0·29	0·75	0·79	0·63	0·68–0·76	1·07	0·97	0·88	0·77
Zr/Nb	3·7	4·2	1·9	1·8	8·8	7·9	3·8	3·0–4·8	32–49		8·8	5·8
Ce/Pb	83	63		64	27	62	33	31–38	17–38	21	21	25
Nb/U	30	31	95	66	29	57	50	40–58	50	41	25	47
Nb/Pb	100	67		127	15	34	25	21–27	7·8	9·8	10·3	15
Th/U	2·5	3·4	2·2	3·7	1·3	2·3	3·7	2·7–4·8	2·5	4·1	3·4	3·9
Ba/La			3·2	6·2	12·3	3·2	6·8		2·5	8·7	12·1	9·5
Zr/Hf	52	55	58	58	49	51	44		36		36	36

MORB is compiled from Sun & McDonough (1989), Woodhead (1996) and Thirlwall (1997); OIB from Sun & McDonough (1989); EM-I and EM-II from Woodhead (1996); HIMU-1 from Mangaia Island (Woodhead, 1996) and HIMU-2 from St. Helena (Thirlwall, 1997).

those from lherzolite in composite xenoliths, also suggesting that the metasomatism of the enriched discrete lherzolites was not caused by fluids similar to those causing the metasomatism of the lherzolites in composite xenoliths, but by CO_2-rich silicate-bearing fluids residual after crystallization of Mg-rich primitive basaltic melts, similar to the process suggested by O'Reilly (1987) and O'Reilly & Griffin (1988).

Relative element diffusion rates in metasomatism

The chemical features of metasomatized peridotites are to a large extent determined by the metasomatic agents. However, metasomatized peridotites sometimes (maybe mostly) cannot reflect completely the nature of metasomatic agents, as the metasomatic process is likely to reflect an open, non-equilibrium system with two-way exchange (e.g. Navon & Stolper, 1987). Reactions between peridotite and metasomatic melts or fluids depend not only on the amount of melts or fluids and their permeability, but also on element diffusion rates. In many cases, the infiltration front of the melts or fluids is distinct from the types of element diffusion fronts described by Bodinier *et al.* (2004).

Figure 13 shows some trace-element variations against Mg-number for clinopyroxenes in the composite xenolith Lz-10. It can be seen from these plots that different elements exhibit different variation patterns. From lherzolite to pyroxenite, Nb, Sr and La contents of clinopyroxenes increase smoothly with decreasing Mg-number, without any compositional discontinuity at the lherzolite–pyroxenite contact (Fig. 13), and these element abundances in lherzolites are markedly enhanced compared with those for depleted lherzolites. This indicates that the exchange of these elements between mafic melt and wall-rock lherzolite was strong and rapid, implying a high diffusion rate. From Ce to Yb, the element abundances between lherzolite and pyroxenite show a gradually increasing compositional break at the contact (Fig. 13a–c). This indicates a slower diffusion rate for these elements. Zr, Hf and Ti abundances decrease significantly from pyroxenite to lherzolite, and their abundances in lherzolite are close to average depleted lherzolite (Fig. 13c and d). There is very limited exchange of Zr, Hf and Ti between lherzolite and pyroxenite, indicating a low diffusion rate. These empirical observations suggest that the geochemical signature of metasomatized peridotites not only depends on element abundances in the metasomatic agent as observed by O'Reilly *et al.* (1991), but also is closely related to element mobility (diffusion rates).

The relative diffusion rate of different elements during metasomatism can be evaluated for these samples. It is assumed that element abundances in the clinopyroxenes in the depleted lherzolites represent the original composition (C^{o}_{px}) for now-metasomatized clinopyroxene, and that the clinopyroxenes in the pyroxenites (C^{b}_{px}) reflect the composition of the metasomatic basanitic melt. Then the relative change (R_m) of element concentration in clinopyroxene (C^{m}_{px}) for the metasomatized lherzolite may be obtained according to following equation:

$$R_m = (C^{m}_{px} - C^{o}_{px})/(C^{b}_{px} - C^{o}_{px}).$$

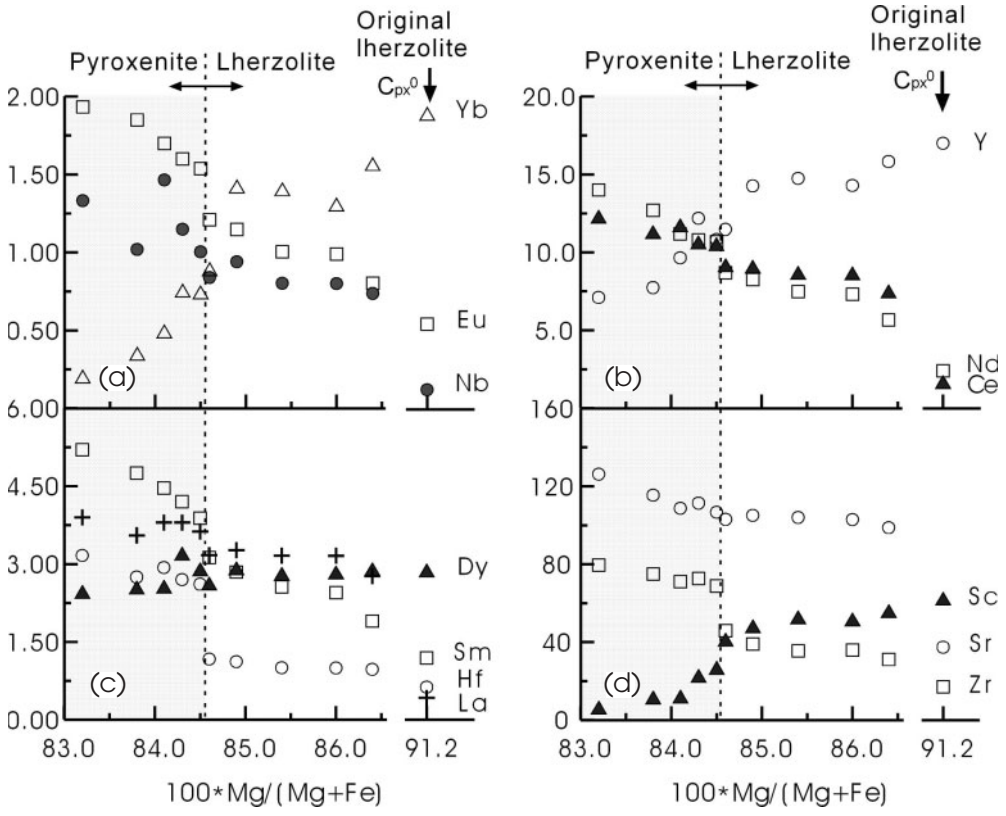

Fig. 13. Trace-element variations of clinopyroxenes from pyroxenite to lherzolite in composite xenolith Lz-10. Distinct variation patterns of the elements imply different diffusive rates in fluid or melt. The 'original lherzolite' at the right end of each plot represents an average value of depleted lherzolites for each element (C_{px}^o; see Table 6 for details).

The higher the value of R_m, the closer the composition of the metasomatized lherzolite is to the composition of metasomatic melt or fluid. Therefore R_m is a measure of the relative diffusion rate of each element during metasomatism. Two suites of R_m data (Table 6) are calculated assuming respectively C_{px}^b equal to the composition of the clinopyroxene most distant from the contact or C_{px}^b equal to the average value of four clinopyroxenes distant from the contact. The latter practice is to avoid random error. Little difference for the trace-element R_m sequences is observed between these two calculations. Results of the calculations for composite xenolith Lz-10 show that Sr, La, Ce and Nb have the highest diffusion rates, whereas Sc, Ga, Zr, Hf and Ti have low diffusion rates. The diffusion rate for the REE decreases from La to Lu, except for the MREE (Gd to Er). Low diffusion rates for the MREE may be due to the similar concentrations of these elements in the original lherzolite (C_{px}^o) and in the metasomatic agent (C_{px}^b), with the consequence of a low chemical potential (e.g. Dy, Fig. 13c).

The calculation demonstrates that the relative mobility of each element in the fluid infiltrating into lherzolites is different, and the order of mobility does not strictly follow the widely accepted incompatibility sequence such as that proposed by Sun & McDonough (1989). Sr has higher mobility than Ce, whereas Nb has a lower mobility. It is noteworthy that Nb, Zr, Hf and Ti show significantly lower diffusive abilities than adjacent REE in the incompatibility sequence for basalts (Sun & McDonough, 1989). Similar conclusions can be obtained based on other composite xenolith data and are analogous to those of Zanetti *et al.* (1996) for veined hornblendite in the Lherz peridotite. Therefore, REE fractionation [$(La/Yb)_n$ ratio] in metasomatized lherzolites could be enhanced significantly by this demonstrated decreasing diffusion rate in the REE from La to Lu.

Therefore, significant HFSE negative anomalies in some metasomatized lherzolites may not simply reflect low contents in metasomatic melts or fluids, but may be due to their lower diffusion rates (compared with REE of similar compatibility) if the metasomatizing system is not in equilibrium. In this case, it would be invalid to calculate the chemical characteristics of model melts using metasomatized mineral compositions, because only the incompatible elements with high diffusion rate might have reached equilibrium between peridotite and metasomatic agent, whereas those with low diffusion rate might not. Hence, the relative diffusion rates of different

Table 6: Relative diffusive ability of trace elements in the metasomatic agent calculated from clinopyroxene compositions of composite xenolith Lz-10

	C^{o}_{px} (ppm)	C^{b}_{px} (ppm)	C^{m}_{px} (ppm)	$R_m(1)$	$R_m(2)$
Sr	37·4	115·6	102·8	0·84	0·74
La	0·42	3·76	3·09	0·80	0·77
Ce	1·68	11·5	8·48	0·69	0·64
Nb	0·12	1·24	0·82	0·63	0·58
Pr	0·35	1·98	1·30	0·58	0·51
Nd	2·40	12·2	7·18	0·49	0·41
Sm	1·19	4·65	2·44	0·36	0·31
Eu	0·54	1·77	0·99	0·36	0·32
Gd	1·99	4·70	2·77	0·29	0·26
Tb	0·41	0·63	0·47	0·29	0·26
Dy	2·88	2·70	2·87	0·06	0·02
Ho	0·67	0·38	0·60	0·25	0·19
Y	17·1	9·18	14·8	0·28	0·23
Er	1·93	0·66	1·54	0·31	0·25
Tm	0·28	0·08	0·21	0·35	0·29
Yb	1·89	0·45	1·43	0·32	0·27
Lu	0·27	0·06	0·20	0·33	0·28
Zr	17·1	74·6	35·4	0·32	0·29
Sc	62·5	13·2	52·1	0·21	0·19
Hf	0·63	2·89	1·02	0·18	0·15
Ti	2205	12601	3879	0·16	0·16
Ga	3·71	19·2	6·12	0·16	0·11

C^{o}_{px}, average value of depleted Leizhou lherzolites (Lz-5, Lz-6, Lz-11, xw97-1, xw97-2, xw97-3, Lz-18 and Lz-19), of which La, Ce and Pr abundance for xw97-1, xw97-3 and Lz-11 were revised to eliminate metasomatic effect; C^{m}_{px}, average values of four clinopyroxenes of lherzolite domain of Lz-10 distant from the contact, representing element abundance of clinopyroxenes after metasomatism; C^{b}_{px}, average of four clinopyroxenes of pyroxenite domain of Lz-10 distant from the contact, representing composition of metasomatic melt or fluid; R_m, relative change in the degree of element enrichment or depletion, reflecting element mobility; $R_m(1)$ is calculated by using the data listed here and $R_m(2)$ is calculated by assuming C^{b}_{px} equal to the composition of clinopyroxene most distant from the contact (see Table 2).

elements are very important to evaluate the geochemical features of the metasomatized peridotites.

CONCLUSIONS

(1) The spinel lherzolites beneath the Leizhou Peninsula (South China) provide evidence that they may represent a coherent asthenospheric column that upwelled probably during Mesozoic lithospheric thinning of South China. The deeper lherzolites are less depleted than the shallow ones, and the compositional sequence from about 60 to 30 km can be modelled as residues of incremental melting grading from about 1% to 11% melting with decreasing depth, and with a melting increment gradient of 1·1%/kbar. The resultant calculated melt volume of potential underplated mafic magmas could account for the majority of the present-day lower crust beneath this region.

(2) Earlier metasomatic effects of young sub-lithospheric mantle upwelling (possibly associated with the opening of the SCSB around 32–15 Ma or an earlier magmatism event) overprinted the mantle lithospheric column previously formed by extension-related asthenospheric upwelling in the Mesozoic, and recent metasomatism is possibly related to early post-spreading magmatism. This is attributed to sub-lithospheric upwelling, but the present data cannot unequivocally distinguish between an upwelling of asthenosphere with a HIMU signature, or a plume [for which there is present-day geophysical evidence from Lebedev & Nolet (2003)].

(3) Some Leizhou Cr-diopside mantle wall-rock lherzolites, especially those in contact with pyroxenites (products of lithospheric intrusions by mafic melts), were strongly metasomatized, resulting in LREE enrichment [especially evident by the large variations in the clinopyroxene $(La/Yb)_n$ ratios (0·05–5·94)], apparent HFSE depletion, and little change in LILE. The parent melt of the pyroxenites (similar to HIMU-type OIB) is inferred to be the main metasomatizing agent (at this time) and to be related to the sub-lithospheric mantle upwelling followed by the opening of the SCSB (32–15 Ma). This metasomatic event overprinted the previously formed lithospheric column shortly before entrainment in the magmas that transported the xenoliths to the surface.

(4) Geochemical characteristics of metasomatized lherzolites reflect not only the composition of metasomatic agents, but also the intensity of metasomatism. Low degrees of metasomatism result in slight enrichment in the more incompatible elements, such as Sr, La, Ce and Nb, but there is little effect on the less incompatible and compatible elements, such as HREE, Y, Ni (and most major elements). Weakly metasomatized lherzolites may not reflect the real geochemical characteristics of the metasomatic agent, because the changes are not pervasive. However, they can be used to model the style and extent of the previous melting depletion process. In contrast, strongly metasomatized lherzolites cannot accurately model early melting process because most element abundances have been modified, including Yb and Y.

(5) The metasomatic reactions in the peridotite parts of composite xenoliths in this study preserved evidence of trace-element disequilibrium that allows assessment of the nature of the metasomatic processes with reference to relative diffusivity. Sr, La, Ce and Nb have the highest

diffusion rates; other REE have moderate rates decreasing from Pr to Lu; and Zr, Hf and Ti have even lower diffusion rates. Because of the demonstrated decreasing diffusion rate from La to Lu (except for the MREE), the $(La/Yb)_n$ of metasomatized lherzolites could be enhanced. Moreover, the lower diffusion rates of Nb, Zr, Hf and Ti (compared with those for relevant REE) may cause distinct HFSE negative anomalies, and thus the metasomatizing agent is not required to be depleted in these elements.

ACKNOWLEDGEMENTS

This work was supported by the NSF of China Grants (Nos 40372087, 40221301 and 40132010) and by Australian Research Council Large, Discovery and Linkage International grants and an Australia–China Institutional Links Program funding (to S.Y.O'R. and W.L.G.). We thank reviewers Lotte Melchior Larsen, Martin Menzies and Michel Grégoire, and editor John A. Gamble for their comments, which greatly improved the manuscript. We also thank Norman Pearson for his expert input to many aspects (especially advice on geothermobarometry and analytical questions), Ashwini Sharma for her expert LA-ICPMS support, and Tom Bradley for polished grain mounts and thin-section preparation. This is Publication 415 from the National Key Centre for Geochemical Evolution and Metallogeny of Continents (www.es.mq.edu.au/GEMOC/).

REFERENCES

Adam, J. & Green, T. H. (1994). The effects of pressure and temperature on the partitioning of Ti, Sr, and REE between amphibole, clinopyroxene and basaltic melts. *Chemical Geology* **117**, 219–233.

Anders, E. & Grevesse, N. (1989). Abundances of the elements: meteoric and solar. *Geochimica et Cosmochimica Acta* **53**, 197–214.

Baker, J., Chazot, G., Menzies, M. & Thirlwall, M. (1998). Metasomatism of the shallow mantle beneath Yemen by the Afar plume—implications for mantle plume, flood volcanism, and intraplate volcanism. *Geology* **26**, 431–434.

Bodinier, J., Menzies, M. A., Shimizu, N., Frey, F. A. & McPherson, E. (2004). Silicate, hydrous and carbonate metasomatism at Lherz, France: contemporaneous derivatives of silicate melt–harzburgite reaction. *Journal of Petrology* **45**, 299–320.

Brey, G. P. & Köhler, T. (1990). Geothermobarometry in four-phase lherzolites: II. New thermobarometers, and practical assessment of existing thermobarometers. *Journal of Petrology* **31**, 1353–1378.

Briais, A., Patriat, P. & Tapponnier, P. (1993). Updated interpretation of magnetic anomalies and seafloor spreading stages in the South China Sea; implications for the Tertiary tectonic of SE China. *Journal of Geophysical Research* **98**, 6299–6328.

Chalot-Prat, F. & Boullier, A.-M. (1997). Metasomatism in the subcontinental mantle beneath the Eastern Carpathians (Romania): new evidence from trace element geochemistry. *Contributions to Mineralogy and Petrology* **129**, 284–307.

Chung, S.-L., Lee, T.-Y., Lo, C.-H., Wang, P.-L., Chen, C.-Y., Yem, N. T., Hao, T. T. & Genyao, W. (1997). Intraplate extension prior to continental extrusion along the Ailao Shan–Red River shear zone. *Geology* **25**, 311–314.

Coltorti, M., Bonadiman, C., Hinton, R. W., Siena, F. & Upton, B. G. J. (1999). Carbonatite metasomatism of the oceanic upper mantle: evidence from clinopyroxenes and glasses in ultramafic xenoliths of Grande Comores, Indian Ocean. *Journal of Petrology* **40**, 133–165.

Cull, J. P., O'Reilly, S. Y. & Griffin, W. L. (1991). Xenolith geotherms and crustal models in eastern Australia. *Tectonophysics* **192**, 359–366.

Flower, M. F. J., Zhang, M. & Chen, C. (1992). Magmatism in the South China Basin: 2. Post-spreading Quaternary basalts from Hainan Island, South China. *Chemical Geology* **97**, 65–87.

Fodor, R. V., Sial, A. N. & Gandhok, G. (2002). Petrology of spinel peridotite xenoliths from northeastern Brazil: lithosphere with a high geothermal gradient imparted by Fernando de Noronha plume. *Journal of South American Earth Sciences* **15**, 199–214.

Forsyth, D. W. (1993). Crustal thickness and the average depth and degree of melting in fractional melting models of passive flow beneath mid-ocean ridges. *Journal of Geophysical Research* **98**, 16073–16079.

Frey, F. A. & Green, D. H. (1974). The mineralogy, geochemistry and origin of lherzolite inclusions in Victorian basanites. *Geochimica et Cosmochimica Acta* **38**, 1023–1059.

Gorring, M. L. & Kay, S. M. (2000). Carbonatite metasomatized peridotite xenoliths from south Patagonia: implications for lithospheric processes and Neogene plateau magmatism. *Contributions to Mineralogy and Petrology* **140**, 55–72.

Grégoire, M., Moine, B. N., O'Reilly, S. Y., Cottin, J. Y. & Giret, A. (2000). Trace element residence and partitioning in mantle xenoliths metasomatized by highly alkaline, silicate- and carbonate-rich melts (Kerguelen Islands, Indian Ocean). *Journal of Petrology* **41**, 477–509.

Harrison, T. M., Leloup, P. H., Ryerson, F. J., Tapponnier, P., Lacassin, R. & Chen, W. (1996). Diachronous initiation of transtension along the Ailao Shan–Red River shear zone, Yunnan and Vietnam. In: Yin, A. & Harrison, T. M. (eds) *The Tectonic Evolution of Asia*. New York: Cambridge University Press, pp. 205–226.

Hart, S. R. & Dunn, T. (1993). Experimental cpx/melt partitioning of 24 trace elements. *Contributions to Mineralogy and Petrology* **113**, 1–8.

Hart, S. R. & Zindler, A. (1986). In search of a bulk-earth composition. *Chemical Geology* **57**, 247–267.

Hirschmann, M. M. & Stolper, E. (1996). A possible role for garnet pyroxenite in the origin of the 'garnet signature' in the MORB. *Contributions to Mineralogy and Petrology* **124**, 185–208.

Hoang, N. & Flower, M. (1998). Petrogenesis of Cenozoic basalts from Vietnam: implication for origins of a 'diffuse igneous province'. *Journal of Petrology* **39**, 369–395.

Ionov, D. A., Ashchepkov, I. V., Stosch, H. G., Witt-Eickschen, G. & Seck, H.A. (1993). Garnet peridotite xenoliths from the Vitim volcanic field, Baikal region: the nature of the garnet–spinel peridotite transition zone in the continental mantle. *Journal of Petrology* **34**, 1141–1175.

Iwamori, H., McKenzie, D. P. & Takahashi, E. (1995). Melt generation by isentropic mantle upwelling. *Earth and Planetary Science Letters* **134**, 253–266.

Johnson, K. T. M., Dick, H. J. B. & Shimizu, N. (1990). Melting in the oceanic mantle: an ion microprobe study of diopsides in abyssal peridotites. *Journal of Geophysical Research* **95**, 2661–2678.

Kepezhinskas, P. K., Defant, M. J. & Drummond, M. S. (1995). Na metasomatism in the island arc mantle by slab melt–peridotite interaction: evidence from mantle xenoliths in the North Kamchatka arc. *Journal of Petrology* **36**, 1250–1267.

Kepezhinskas, P. K., Defant, M. J. & Drummond, M. S. (1996). Progressive enrichment of island arc mantle by melt–peridotite interaction inferred from Kamchatka xenoliths. *Geochimica et Cosmochimica Acta* **60**, 1217–1229.

Klemme, S., Van der Laan, S. R., Foley, S. F. & Gunther, D. (1995). Experimental determined trace and minor element partitioning between clinopyroxene and carbonatite melt under upper mantle conditions. *Earth and Planetary Science Letters* **133**, 439–448.

Langmuir, C. H., Klein, E. M. & Plank, T. (1992). Petrological systematics of mid-ocean ridge basalts: constraints on melt generation beneath ocean ridge. In: Phipps Morgan, J., Blackman, D. K. & Sinton, J. M. (eds) *Mantle Flow and Melt Generation at Mid-Ocean Ridges. American Geophysical Union Monograph* **71**, 183–280.

Larsen, L. M., Pedersen, A. K., Sundvoll, B. & Frei, R. (2003). Alkali picrites formed by melting of old metasomatized lithospheric mantle: Mantdlat Member, Vaigat Formation, Palaeocene of West Greenland. *Journal of Petrology* **44**, 3–38.

La Tourrette, T., Hervig, R. L. & Holoway, J. R. (1995). Trace element partitioning between amphibole, phlogopite, and basanite melt. *Earth and Planetary Science Letters* **135**, 13–30.

Lebedev, S. & Nolet, G. (2003). Upper mantle beneath southeast Asia from *S* velocity tomography. *Journal of Geophysical Research* **108**(B1): 2048, doi: 10.1029/2000JB000073.

Lin, Z., Hu, H., Zhu, L., Chen, X., Zhang, S., Zhu, Z. & Liao, Q. (1988). Preliminary study of the crustal structure of Lei-Qiong area. In Ding, Y. Z. (ed.) *Seismic Study of Northern Hainan Island*. Beijing: Seismic Press, pp. 127–139 (in Chinese).

Litasov, K. D., Foley, S. F. & Litasov, Y. D. (2000). Magmatic modification and metasomatism of the subcontinental mantle beneath the Vitim volcanic field (East Siberia): evidence from trace element data on pyroxenite and peridotite xenoliths from Miocene picrobasalt. *Lithos* **54**, 83–114.

Liu, C. Q., Masuda, A. & Xie, G. H. (1994). Major- and trace-element compositions of Cenozoic basalts in eastern China: petrogenesis and mantle source. *Chemical Geology* **114**, 19–42.

McDonough, W. F. & Sun, S. S. (1995). The composition of the earth. *Chemical Geology* **120**, 223–253.

McKenzie, D. (1984). The generation and compaction of partially molten rock. *Journal of Petrology* **25**, 713–765.

McKenzie, D. & Bickle, M. J. (1988). The volume and composition of melt generated by extension of the lithosphere. *Journal of Petrology* **29**, 625–679.

McKenzie, D. & O'Nions, R. K. (1991). Partial melt distributions from inversion of rare earth element concentration. *Journal of Petrology* **32**, 1021–1091.

Menzies, M. A., Rodgers, N., Tindle, A. & Hawkesworth, C. J. (1987). Metasomatic and enrichment processes in lithospheric peridotites, and effect of asthenosphere–lithosphere interaction. In: Menzies, M. A. & Hawkesworth, C. J. (eds) *Mantle Metasomatism*. London: Academic Press, pp. 313–361.

Navon, O. & Stolper, E. (1987). Geochemical consequences of melt percolation: the upper mantle as a chromatographic column. *Journal of Geology* **95**, 285–308.

Neumann, E.-R., Griffin, W. L., Pearson, N. J. & O'Reilly, S. Y. (2004). The evolution of the upper mantle beneath the Canary Islands: information from trace elements and Sr isotope ratios in minerals in mantle xenoliths. *Journal of Petrology* **45**, 2573–2612.

Niu, Y. (1997). Mantle melting and melt extraction processes beneath ocean ridges: evidence from abyssal peridotites. *Journal of Petrology* **38**, 1047–1074.

Norman, M. D. (1998). Melting and metasomatism in the continental lithosphere: laser ablation ICPMS analysis of minerals in spinel lherzolites from eastern Australia. *Contributions to Mineralogy and Petrology* **130**, 240–255.

O'Reilly S. Y. (1987). Volatile-rich mantle beneath eastern Australia. In: Nixon, P. H. (ed.) *Mantle Xenoliths*. Chichester: John Wiley, pp. 661–670.

O'Reilly, S. Y. & Griffin, W. L. (1988). Mantle metasomatism beneath western Victoria, Australia: I. Metasomatic processes in Cr-diopside lherzolites. *Geochimica et Cosmochimica Acta* **52**, 433–447.

O'Reilly, S. Y., Griffin, W. L. & Ryan, C. G. (1991). Residence of trace elements in metasomatized spinel lherzolite xenoliths: a proton-microprobe study. *Contributions to Mineralogy and Petrology* **109**, 98–113.

Powell, W., Zhang, M., O'Reilly, S., Y. & Tiepolo, M. (2004). Mantle amphibole trace-element and isotopic signatures trace multiple metasomatic episodes in lithospheric mantle, western Victoria, Australia. *Lithos* **75**, 141–171.

Riley, G. N. & Kohlstedt, D. L. (1991). Kinetics of melt migration in upper mantle-type rocks. *Earth and Planetary Science Letters* **105**, 500–521.

Rudnick, R. L., McDonough, W. F. & Chappell, B. W. (1993). Carbonatite metasomatism in the northern Tanzanian mantle: petrographic and geochemical characteristics. *Earth and Planetary Science Letters* **114**, 463–475.

Salters, V. J. M. & Shimizu, N. (1988). World-wide occurrence of HFSE-depleted mantle. *Geochimica et Cosmochimica Acta* **52**, 2177–2182.

Schiano, P., Clocchiatti, R., Shimizu, N., Maury, R. C., Jochum, K. P. & Hofmann, A.W. (1995). Hydrous, silica-rich melts in the sub-arc mantle and their relationship with erupted arc lavas. *Nature* **377**, 595–600.

Shen, Y. & Forsyth, D. W. (1995). Geochemical constraints on initial and final depths of melting beneath mid-ocean ridges. *Journal of Geophysical Research* **100**, 2211–2237.

Sun, M. & Kerrich, R. (1995). Rare earth element and high field strength element characteristics of whole rocks and mineral separats of ultramafic nodules in Cenozoic volcanic vents of southeastern British Columbia, Canada. *Geochimica et Cosmochimica Acta* **59**, 4863–4879.

Sun, S. S. & McDonough, W. F. (1989). Chemical and isotopic systematics of oceanic basalts: implications for mantle composition and processes. In: Saunders, A. D. & Norry, M. J. (eds) *Magmatism in the Ocean Basins. Geological Society, London, Special Publications* **42**, 313–345.

Tapponnier, P., Peltzer, G. & Armijo, R. (1986). On the mechanics of the collision between India and Asia. In: Coward, M. P. & Ries, A. C. (eds) *Collision Tectonics. Geological Society, London, Special Publications* **19**, 115–157.

Taylor, B. & Hayes, D. E. (1983). Origin and history of the South China Basin. In: Hayes, D. E. (ed.) *The Tectonic and Geologic Evolution of Southestern Asian Seas and Islands, Part 2. American Geophysical Union Monograph* **27**, 23–56.

Thirlwall, M. F. (1997). Pb isotopic and elemental evidence for OIB derivation from young HIMU mantle. *Chemical Geology* **139**, 51–74.

Tu, K., Flower, M. F. J., Carlson, R. W., Xie, G., Chen, C. & Zhang, M. (1992). Magmatism in the South China Basin 1. Isotopic and trace element evidence for an endogenous Dupal mantle component. *Chemical Geology* **97**, 47–63.

Vannucci, R., Bottazzi, P., Wulff-Pedersen, E. & Neumann, E. R. (1998). Partitioning of REE, Y, Sr, Zr and Ti between clinopyroxene and silicate melts in the mantle under La Palma (Canary Islands): implications for the nature of the metasomatic agents. *Earth and Planetary Science Letters* **158**, 39–51.

Wang, P.-L., Lo, C.-H., Lee, T.-Y., Chung, S.-L., Lan, C.-Y. & Yem, N. T. (1998). Thermochronological evidence for the movement of

the Ailao Shan–Red River shear zone: a perspective from Vietnam. *Geology* **26**, 887–890.

Wang, W. & Gasparik, T. (2001). Metasomatic clinopyroxenes in diamonds from the Lianing province, China. *Geochimica et Cosmochimica Acta* **65**, 611–620.

Wiechert, U., Ionov, D.A. & Wedepohl, K. H. (1997). Spinel peridotite xenoliths from the Atsagin-Dush volcano, Dariganga lava plateau, Mongolia: a record of partial melting and cryptic metasomatism in the upper mantle. *Contributions to Mineralogy and Petrology* **126**, 345–364.

Woodhead, J. D. (1996). Extreme HIMU in an oceanic setting: the geochemistry of Mangaia Island (Polynesia), and temporal evolution of the Cook–Austral hotspot. *Journal of Volcanology and Geothermal Research* **72**, 1–19.

Xu, X., O'Reilly, S. Y., Griffin, W. L. & Zhou, X. (2000). Genesis of young lithospheric mantle in southeastern China: an LAM-ICPMS trace element study. *Journal of Petrology* **41**, 111–148.

Xu, X., O'Reilly, S. Y., Griffin, W. L. & Zhou, X. (2003). Enrichment of upper mantle peridotite: petrological, trace element and isotopic evidence in xenoliths from SE China. *Chemical Geology* **198**, 163–188.

Xu, Y. F., Zhu, Z. H., Wen, Q., Wen, G. & Pu, Z. H. (1999). Clay mineral, chemical characteristics and environmental record of the multi-stage laterite at Yingfengling section, Leizhou Peninsula. *Geochimica* **28**, 281–288 (in Chinese with English abstract).

Yan, P., Zhou, D. & Liu, Z. (2001). A crustal structure profile across the northern continental margin of the South China Sea. *Tectonophysics* **338**, 1–21.

Yang, H. J., Sen, G. & Shimizu, N. (1998). Mid-ocean ridge melting: constraints from lithospheric xenoliths at Oahu, Hawaii. *Journal of Petrology* **39**, 277–295.

Yao, B., Zeng, W., Chen, Y., Zhang, X., Hayes, D. E., Diebold, J., Buhl, P. & Spangler, S. (1994). The crustal structure in the eastern part of the northern margin of the South China Sea. *Acta Geophysica Sinica* **37**, 27–35 (in Chinese with English abstract).

Yaxley, G. M., Green, D. H. & Kamenetsky, V. (1998). Carbonatite metasomatism in the southeastern Australian lithosphere. *Journal of Petrology* **39**, 1917–1930.

Yu, J.-H. & O'Reilly, S. Y. (2001). Almandine megacrysts from Yingfengling Cenozoic basalt in Leizhou Peninsula and their parental magma origin. *Chinese Science Bulletin* **46**, 2013–2018.

Yu, J.-H., O'Reilly, S. Y., Griffin, W. L., Xu, X., Zhang, M. & Zhou, X. (2003*a*). The thermal state and composition of lithospheric mantle beneath Leizhou Peninsula, South China. *Journal of Volcanology and Geothermal Research* **122**, 165–189.

Yu, J.-H., O'Reilly, S. Y. & Zhou, X. (2003*b*). Geochemistry of clinopyroxene megacrysts from Yingfengling basalt and the metasomatism effect of their parental magma on mantle peridotites. *Acta Petrologica Sinica* **19**, 637–649 (in Chinese with English abstract).

Yu, J.-H., Xu, X. S., O'Reilly, S. Y., Griffin, W. L. & Zhang, M. (2003*c*). Granulite xenoliths from Cenozoic basalts in SE China provide geochemical fingerprints to distinguish lower crust terranes from the North and South China tectonic blocks. *Lithos* **67**, 77–102.

Zanetti, A., Vannucci, R., Bottazzi, P., Oberti, R. & Ottolini, L. (1996). Infiltration metasomatism at Lherz as monitored by systematic ion-microprobe investigations close to a hornblendite vein. *Chemical Geology* **134**, 113–133.

Zangana, N. A., Downes, H., Thirlwall, M. F., Marriner, G. F. & Bea, F. (1999). Geochemical variation in peridotite xenoliths and their constituent clinopyroxenes from Ray Pic (French Massif Central): implications for the composition of the shallow lithospheric mantle. *Chemical Geology* **153**, 11–35.

Zhu, B. & Wang, H. (1989). Nd–Sr–Pb isotopic and chemical evidences for the volcanism with MORB–OIB source characteristics in the Leiqiong area, China. *Geochimica* (3), 193–201 (in Chinese with English abstract).

Zou, H., Kindler, A., Xu, X. & Qi, Q. (2000). Major, trace element, and Nd, Sr and Pb isotope studies of Cenozoic basalts in SE China: mantle sources, regional variations, and tectonic significance. *Chemical Geology* **171**, 33–47.